Regimes of Dry Convection above Wildfires: Idealized Numerical Simulations and Dimensional Analysis*

MICHAEL T. KIEFER AND MATTHEW D. PARKER

North Carolina State University, Raleigh, North Carolina

JOSEPH J. CHARNEY

Northern Research Station, USDA Forest Service, East Lansing, Michigan

(Manuscript received 22 July 2008, in final form 3 October 2008)

ABSTRACT

Wildfires are capable of inducing atmospheric circulations that result predominantly from large temperature anomalies produced by the fire. The fundamental dynamics through which a forest fire and the atmosphere interact to yield different convective regimes is still not well understood. This study uses the Advanced Regional Prediction System (ARPS) model to investigate the impact of the environmental (i.e., far upstream, undisturbed by fire) wind profile on dry convection above a prescribed heat source of an intensity and spatial scale comparable to a wildfire. Dimensional analysis of the fire–atmosphere problem provides two relevant parameters: a surface buoyancy parameter that addresses the amount of heat a parcel of air receives in transiting above the fire and an advection parameter that addresses the degree to which the environmental wind advects updrafts away from the fire. Two-dimensional simulations are performed in which the upstream surface wind speed and mixed layer mean wind speed are varied independently to better understand the fundamental processes governing the organizational mode and updraft strength.

The result of these experiments is the identification of two primary classes of dry convection: plume and multicell. Simulated plume cases exhibit weak advection by the mean wind and are subdivided into intense plume and hybrid classes based on the degree of steadiness within the convection column. Hybrid cases contain columns of largely discrete updrafts versus the more continuous updraft column associated with the intense plume mode. Multicell cases develop with strong mixed layer advection and are subdivided into strong and weak classes based on the depth of convection. Intense plume and strong multicell (hybrid and weak multicell) cases occur when the surface buoyancy is large (small). Parcel analyses are performed to more closely examine the forcing of convection within different areas of the parameter space. The multicell (strong and weak) and intense plume modes are forced by a combination of buoyancy and dynamic pressure gradient forcing associated with the perturbation wind field, whereas the hybrid mode is forced by a combination of buoyancy and dynamic pressure gradient forcing associated with the strong background shear.

The paper concludes with a discussion of the degree of nonlinearity that is likely to exist at the fire front for each of the convective modes; nonlinear fire behavior is most likely for the hybrid mode and least likely for the weak multicell mode. Knowledge of the sensitivity of the convective mode to upstream conditions can provide information about the degree of nonlinear or erratic fire behavior expected for a given wind profile upstream of the fire.

1. Introduction

Wildfires can have a profound impact on atmospheric circulations, primarily through temperature anomalies that result from the release of energy due to the combustion of organic material. Sensible heat fluxes of 0.8–2 MW m^{-2}, in combination with the moisture produced during the combustion process, can produce buoyancy-driven horizontal and vertical circulations that feed back on the fires via the advection of hot gases and burning material and also through the mixing of air with

* Supplemental information related to this paper is available at the Journals Online Web site: http://dx.doi.org/10.1175/2009JAS2896.s1.

Corresponding author address: Michael Kiefer, Department of Marine, Earth, and Atmospheric Sciences, North Carolina State University, Raleigh, NC 27695.
E-mail: mtkiefer@ncsu.edu

DOI: 10.1175/2008JAS2896.1

© 2009 American Meteorological Society

flames to increase flame temperature and subsequently fire intensity (Jenkins et al. 2001). Early numerical modeling studies of plumes above forest fires considered only the gross plume characteristics, the result of which was a broad classification of plume-dominated and wind-driven fires, with weaker (stronger) mean winds and greater (lesser) heat output associated with the former (latter) (Byram 1959; Grishin et al. 1984). Plume-dominated fires feature more upright plumes whereas wind-driven fires are associated with plumes strongly tilted downstream. Note, however, that this classification is purely qualitative in that there is no rigorous, quantitative measure that differentiates between plume-dominated and wind-driven wildfires.

The interaction of the environmental (i.e., unperturbed, far upstream) wind with buoyant circulations above wildfires, however, can lead to the development of multiple modes of convection of varying intensity and spatiotemporal scale. The fundamental dynamics behind the development of these convective modes are still not well understood. One such convective mode is multicellular convection, which consists of convective cells that periodically develop and propagate away from the fire. A second mode of interest is the fire plume, which consists of one large, generally upright convection column with strong vertical velocities. Each of these phenomena has appeared in lidar observations (see Banta et al. 1992, Figs. 4 and 8) and in numerical simulations using a coupled fire–atmosphere model (see Clark et al. 1996b, Fig. 9). It should be noted that the focus of Clark et al. (1996b) was on the multiscale processes that control certain aspects of fire behavior, such as fire line shape and spread rate. Although different convective modes were apparent in the figures presented by Clark et al. (1996b), the features were not examined in detail. In this study, we are interested in the characteristics and dynamics of these phenomena.

Multicellular convection is a phenomenon that has been studied in depth through both observations and numerical simulations for more than 30 years [see brief reviews in Lin et al. (1998) and Fovell and Tan (1998)]. The classic model of multicell convection involves a cold pool resulting from precipitation falling into dry subcloud air, which generates an updraft at its leading edge. Discrete updraft cells periodically separate from the gust front and move rearward (with respect to storm motion) over the cold pool, depositing precipitation into the dry subcloud air and thereby sustaining the mesoscale convective system. A number of theories have been developed to explain why cells separate from the leading edge of the cold pool (i.e., the gust front) or, in other words, why the convection is multicellular rather than unicellular. Lin et al. (1998) proposed an advection-cutoff mechanism whereby compensating subsidence flanking the cell cuts the cell off from the gust front updraft. Fovell and Tan (1998) concluded that buoyant circulations associated with growing cells could weaken the gust front updraft and mix stable environmental air into the cells inflow, effectively cutting the cell off from its convective forcing and allowing advection to control cell movement away from the gust front. Kiefer et al. (2008), in a numerical modeling study, simulated both plume and multicell modes generated by forest fires and found that the fire-induced multicell mode is essentially a series of buoyant bubbles that are advected by the environmental flow. With the relatively weak heat source and large mean wind used in the Kiefer et al. (2008) simulations, updrafts were unable to strengthen substantially before being advected away from the surface heat source.

In contrast, the unicellular wildfire plume mode has been given much less attention in terms of the dynamics of mode development, despite the fact that the most intense three-dimensional phenomena are associated with single plumes as opposed to multicell convection. Much greater attention has been given to processes on the scale of the fire line width [O(100 m)] or smaller (e.g., Clark et al. 1996a; Cunningham et al. 2005), processes that are of vital importance to operations at the fire front. It is, however, important to consider the dynamics of the intense plume convection because atmospheric circulations with scales O(1 km) may significantly affect conditions at the fire line (Potter 2005). Over the past 50 yr, much of the research considering the role of the environmental wind in single plume dynamics has focused on the upright versus tilted structure of plumes in relation to ambient wind speed. Recently, Kiefer et al. (2008) examined the role of a wind reversal and Kelvin–Helmholtz instability in generating intense plume phenomena in conditions that would normally be associated with multicell convection (i.e., weak surface heat fluxes and strong winds). More work, however, is needed to examine intense plume dynamics in different environments.

Although three-dimensional phenomena such as buoyancy-generated vortices will not be directly addressed in this study, some review is justified because of the association of such phenomena with fire plumes. McRae and Stocks (1987) and McRae and Flannigan (1990) describe fire-driven vertical vortices strong enough to rip out standing trees and clear surface organic material, exposing bare mineral soil underneath. Simard et al. (1983) describe firefighter observations of what appear to have been horizontal roll vortices that locally perturbed the wind field and produced intense downdrafts in the early stages of the May 1980 Mack Lake fire

in northern lower Michigan. The unpredictable movement of the fire and lofting of firebrands (burning material) led to the ignition of new fires and the death of a firefighter suddenly caught between the primary and secondary fires. Additionally, McRae and Flannigan (1990) detail 20 occurrences of vertical vortices, some growing to 400 m in diameter and persisting for as long as 2 h before dissipating during a 5-yr period of prescribed fires in Ontario, Canada. Given that intense vortical phenomena are most commonly associated with fire plumes, an improved understanding of the balance between buoyancy and upstream flow that yields strong plumes (versus multicells) should be of interest to the firefighting community.

We hypothesize that two fundamental processes determine the organizational mode and overall intensity of convection: advection by the upstream wind through the depth of the mixed layer and the heating of surface air parcels by the fire. These processes can be encapsulated in two nondimensional parameters that act as control parameters for dry convection generated by forest fires. These control parameters will be shown to be of use in predicting organizational mode and intensity. By fixing surface heat flux, heating diameter, and mixed layer depth, the sensitivity of convective mode to the surface wind speed and mixed layer mean wind speed can be rigorously examined. This approach to the fire-induced convection problem is similar to that of Baik et al. (2001), who explored the linear and weakly nonlinear regimes of convection above urban heat islands in stably stratified environments. Linear gravity waves were found to develop for weaker heating and stronger basic state wind speed, and both gravity waves and an updraft cell were found to develop for stronger heating and weaker basic state wind speed. The much smaller horizontal scale and larger amplitude of heating in the fire problem motivates a study of regimes for varying upstream conditions (and heating amplitudes) associated with wildfires.

To minimize complexity, numerical simulations in this study do not address how atmospheric circulations feed back on the fire to perturb the fire line shape/speed or promote the ignition of new fires. More sophisticated coupled fire–atmosphere models have been developed that are better suited for examining the impact of multiscale circulations on fire line speed, shape, and intensity (e.g., Clark et al. 1996a; Linn et al. 2002; Sun et al. 2009). The utility of the highly simplified model design used in this study is in allowing fundamental atmospheric processes controlled by the environmental wind field and heat flux from a fire to be examined with minimal complications. The potential impacts of each convective mode on a pre-existing fire line and/or new fires will, however, be discussed, with the implication that although great complexity is involved at the scales of the fire itself, knowledge of the background (i.e., unperturbed) wind profile can provide a warning as to how unpredictable and violent a fire may become. It should be noted, however, that only two-dimensional flow is considered in this study; the interaction of fire and atmosphere involves greater complexity in a fully three-dimensional flow. Future work will examine regimes of wildfire convection in three-dimensional flows.

A brief literature review of scale analysis of wildfire convection and a description of the new control parameters proposed here are presented in section 2 of this paper. A description of the numerical model used in this study and the experiment design are presented in section 3. Results and discussion of the matrix of experiments and potential impacts of each convective mode on wildfires are presented in sections 4 and 5, respectively, and the paper is concluded in section 6.

2. Scaling parameters

Attempts have been made in past studies to reduce the problem of forest fire–induced convection to a few governing parameters. Byram (1959) developed two parameters for an infinitesimally narrow fire line. The first parameter, P_w, represents the horizontal flow of kinetic energy through a unit vertical area of the atmosphere at height z (proportional to the cube of the wind speed) and the second, P_f, the rate at which thermal energy is converted into kinetic energy in the convection column over the fire. The ratio of these two, P_f/P_w, was interpreted by Byram as an energy criterion that, when less than unity, indicates the dominance of the environmental wind field over vertical convection and more predictable fire behavior (e.g., spread rate, intensity, flame length and height). The inverse of this parameter has also been interpreted as a Froude number (Nelson 1993). Byram (1966) extended the parameter study to the problem of large, intensely burning fires known as mass fires, with studies by Grishin et al. (1984) and Clark et al. (1996b) developing and applying similar parameters to numerical simulations of fires. The study by Clark et al. (1996b) utilized a form of Froude number such that the thermal energy term is proportional to the deviation of potential temperature above the fire from ambient conditions. A substantial difficulty with this form of the Froude number is the inability to control the thermal energy component of the problem because of the sensitivity of the potential temperature perturbation to low-level wind speed and turbulent diffusion.

Two parameters have been developed in this study to address the two fundamental processes of mixed layer

advection and surface parcel heating: an advection parameter,

$$A^{-1} = \left(\frac{\rho_r' g L^2}{\rho_r \bar{U}^2 L_z}\right), \tag{1}$$

and a surface parcel heating parameter,

$$B = \left(\frac{Q_o L}{U_s \theta_r' L_z \rho_o C_p}\right), \tag{2}$$

where Q_o is the surface heat flux, θ_r' is a perturbation potential temperature scale, and ρ_r and ρ_r' are scales of total and perturbation air density, respectively; $\bar{U}$ and U_s are the far upstream mixed layer mean wind speed and surface wind speed, respectively, and L and L_z are horizontal and vertical length scales of the problem, respectively. All other symbols have standard definitions. The complete derivation of the control parameters is included as supplemental material to this manuscript (available at the Journals Online Web site: http://dx.doi.org/10.1175/2009JAS2896.s1).

Note that there is a degree of freedom in specifying the level at which the buoyancy is calculated in A. It is clear that entrainment of environmental fluid into a growing buoyant plume will result in a large reduction of θ' from values immediately above the heat source. Anecdotal accounts and coupled fire–atmosphere model results suggest reductions of θ' of about two orders of magnitude within the 15–20 m above the combustion region (Potter 2005; Clark et al. 1996b). Reductions in θ' and therefore buoyancy (θ_g'/θ_o) cited by Potter (2005) and Clark et al. (1996b) are consistent with the variation of buoyancy with height within axisymmetric turbulent plumes in uniform environments (Turner 1973). Using dimensional analysis and conservation equations for mass and momentum, Turner showed that buoyancy should vary as $z^{-5/3}$ above a steady point source of buoyancy in a homogenous fluid, suggesting a reduction of two orders of magnitude in θ' over a depth of 20 m.

A range of options exists for choosing the appropriate level at which to determine buoyancy. Using surface buoyancy in Eq. (1) neglects the effects of entrainment and will result in a value of A strongly suggestive of weak advection, regardless of the strength of the mean wind speed. Conversely, using a value of postentrainment buoyancy [e.g., $O(100)$ reduction] will result in a very large value of A for most fires, even those with strong surface heat flux. Advanced Regional Prediction System (ARPS) model experiments with a range of upstream environments suggest an order of magnitude reduction from surface buoyancy over a depth of 15–20 m. The depth of 15–20 m is consistent with the turbulent length scale $L_z \sim \sqrt{K_{m_3} L/(U_\infty P_R)}$, determined from scaling the thermodynamic equation (see the appendix for a definition of scales). The turbulent length scale in this study is probably larger than for most real world fires (e.g., Potter 2005) or prior modeling (e.g., Clark et al. 1996b) because of the larger dimension of the fire in this study. The large fire dimension was necessary to resolve the heating with a reasonable number of grid points while keeping computational demands manageable with 50-m horizontal grid spacing. The form of parameter A applied in this study is

$$A^{-1} = \left|\left[\frac{\frac{1}{10}(\rho_r')_{z\approx 0}}{\rho_o + \frac{1}{10}(\rho_r')_{z\approx 0}}\right]\right| \left(\frac{gL^2}{\bar{U}^2 L_z}\right)_{\mathrm{ML}} \approx \frac{1}{10}\left(\frac{L_z Q_o}{\rho_o C_p \theta_o K_h}\right)_{z\approx 0}\left(\frac{gL^2}{\bar{U}^2 L_z}\right)_{\mathrm{ML}}, \tag{3}$$

where K_h is the eddy diffusivity coefficient, θ_o is a background surface potential temperature, ML is mixed layer, and all other scales are as defined earlier. The order of magnitude reduction in parcel buoyancy in Eq. (3) yields A values on the order of unity, a favorable result for dimensional analysis because neither advection or buoyancy completely dominates A.

The buoyancy parameter is inversely proportional to the surface wind speed, whereas the advection parameter is proportional to the square of the mean mixed layer wind speed. These two parameters thus indicate that for a given change to the surface heat flux, the wind profile through the depth of the plume cannot be adjusted uniformly if one wishes to maintain both A and B parameter similarity. This implies that vertical wind shear is required for advection and that surface buoyancy should be similar between two fires with different magnitudes of surface heat flux, although there is no limitation on the vertical distribution of the wind shear. The role of vertical wind shear in dynamics will be addressed in section 4b. Simulations in which A and B are both held constant, requiring an adjustment to vertical wind shear, are left to future work.

3. Model description and experiment design

The numerical model utilized for this study is the Advanced Regional Prediction System version 5.1.0 (Xue et al. 2000, 2003). ARPS is a three-dimensional, compressible, nonhydrostatic cloud model. Open lateral boundaries are utilized to allow disturbances to exit the computational domain. For our simulations, ARPS has a horizontally homogeneous initial condition. The upper boundary condition for all simulations is a sponge

layer beginning at 6.1 km above the surface and extending up to the top boundary at 10 km. A 1.5-order turbulent kinetic energy (TKE) subgrid-scale turbulence closure scheme is utilized; however, surface radiation physics and surface momentum fluxes are omitted. As regards surface momentum fluxes, proper values of drag coefficients applicable to wildfires are not well known (Cunningham et al. 2005). Drag coefficients vary greatly depending on the details of the fuels (e.g., grasslands versus densely packed pine trees), and the typical method of accounting for static stability effects on surface drag (Monin–Obukhov similarity theory; Stull 1988; Arya 2001) may not be applicable to strong heating scenarios such as wildfires. For these reasons, the methodology adopted here is to address the impacts of surface heat flux first, with investigation of the potential impacts of momentum flux left for future work. Additionally, the Coriolis force is neglected in these simulations because it has a negligible impact on the short-lived convection of the type considered in this study. Fourth-order accurate finite differencing of the advection terms is used in both the vertical and horizontal. The resulting model, while quite simple, is well suited to examining the fundamental dry convective processes with minimal ambiguity.

A two-dimensional computational domain has been utilized with uniform horizontal grid spacing of 50 m in the horizontal and average grid spacing of 40 m in the vertical. Stretching is applied along the vertical axis with finest grid spacing near the surface [$(\Delta z)_{\min} = 2.5$ m]. The model domain extends 40 km in the x direction and 10 km in the z direction. With a domain of 40 km and Orlanski-type open lateral boundary conditions, wave reflections from lateral boundaries have been minimized. The base state profile of Brunt–Väisälä frequency (N) is presented in Fig. 1a with mixed layer N1 = 0.0012 s^{-1} and free atmosphere N2 = 0.013 s^{-1}. The deep, nearly dry adiabatic layer in the ARPS sounding is consistent with an environment conducive to fire development (Werth and Ochoa 1993). Extension of this work to a low-level environment with stable stratification is left for future work. Additional simulations were run with a fully three-dimensional version of ARPS. Although minor differences were noted between the 2D and 3D simulations, in general the modes were reproduced in the 3D model. Future work will further explore the 3D dynamics that appear to add complexity to rather than overwhelm the simple 2D processes considered in this study.

Although the surface heat flux applied in the model is fixed spatially, all fields in this study will be analyzed in a fire-relative framework. To accomplish this, an unspecified fire spread rate S_f is subtracted from the

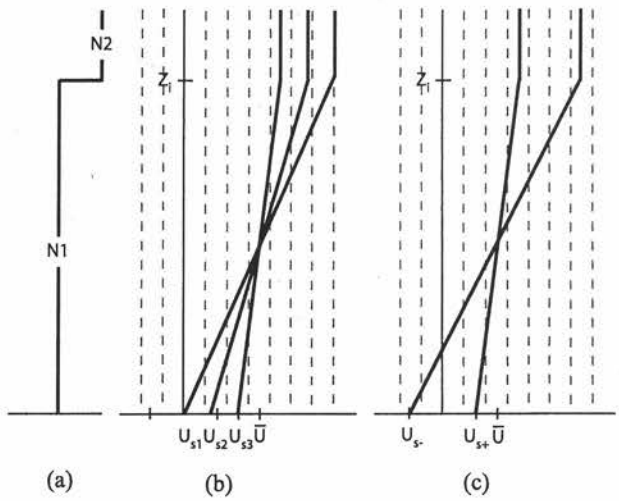

FIG. 1. Generic fire-relative base state wind and static stability profiles. (a) Brunt–Väisälä frequency profile for all cases, where N1 = 0.0012 s^{-1} and N2 = 0.013 s^{-1}. (b) Three example wind profiles with identical mixed layer mean wind $\overline{U}$ and three different values of surface wind speed U_s, but identical surface wind direction. (c) Example wind profiles for two cases with identical $\overline{U}$ and U_s, but opposite surface wind directions such that a wind reversal exists in the profile.

ground relative base-state wind $\hat{U}(z)$ to yield a fire relative base-state wind $U(z)$. A matrix of experiments has been constructed in which the fire-relative surface wind speed U_s and mixed layer mean wind speed $\bar{U}$ are varied independently, while a steady surface heat flux of magnitude 28.8 kW m^{-2} and radius of 260 m is applied at a fixed position in the center of the domain. To limit the cases to a reasonable number, only wind profiles with positive (i.e., westerly) mean wind and vertical wind shear are used; examination of other parts of the parameter space is left to future work. A total of 54 unique $\bar{U} - U_s$ combinations are examined with nine variations of U_s and six variations of $\bar{U}$. Given that fire spread rates typically range from 0.1 to 1 m s^{-1} (Jenkins et al. 2001) and fire-relative winds are expected to differ from ground-relative winds by at most 1 m s^{-1}, the conclusions from this study should apply to situations in which only the upstream, ground-relative wind speed is known. Finally, the magnitude of heat flux specified in the model is representative of a surface fire of moderate intensity, falling within the range of values applied in contemporary idealized modeling of wildland fires (Cunningham et al. 2005, 14 kW m^{-2}; Heilman and Fast 1992, 37 kW m^{-2}; Sun et al. 2006a, 150 kW m^{-2}). It is worth noting that the Sun et al. (2006a) study accounted for radiation loss to surroundings by assuming that roughly 30% of surface heat flux from the fire is unavailable for atmospheric heating; radiative loss is not accounted for in this study. Although observations of

vertical heat fluxes from wildfires are limited, the available data support the use of heat fluxes of this magnitude (e.g., Clements et al. 2007).

Here, U_s and $\bar{U}$ are varied between 0 and 12.5 m s^{-1}, resulting in ranges of parameter A from 0 to 6.8 and parameter B from 0 to ∞. Matrix elements are referred to in this paper as AaBb, where the index a refers to the row and the index b refers to the column of the matrix in Fig. 3. For example, the element A2B2 refers to row 2, column 2 of the experiment matrix, where A = 0.3 and B = 0.4. The base state wind profile consists of positive $\bar{U}$ with constant shear from the surface to the top of the mixed layer Z_i (Fig. 1b). Above Z_i, uniform wind speed and direction is maintained up to the top boundary. Although base state mixed layer wind shear is not controlled in these experiments, our results strongly suggest that updraft intensity is more sensitive to U_s than to ΔU. This was determined by overlaying mode classification and surface wind speed on a $\bar{U} - \Delta U$ matrix; the axis of strong multicell classifications was found to coexist with the $U_s = 0$ axis and the strong/weak multicell boundary was found to align closely with the $U_s = 5$ m s^{-1} contour. No consistent relationship was found between updraft strength and mixed layer wind shear. However, as will be discussed later, analyses do indicate a dynamical role for shear in plume intensity for a number of cases.

The substantial shear in some of the mixed layer wind profiles in this study requires further examination to understand how the development of a realistic boundary layer might affect results. In additional experiments, the boundary layer was allowed to develop in a 3D model with an environmental surface heat flux of magnitude 200 W m^{-2}, reasonable for a clear day (Stull 1988). The mean wind profile that develops after the turbulence reaches a quasi-steady state was extracted and then used as the base state wind profile for 2D simulations with a fire heat flux (but no environmental surface heat fluxes). This was performed for the A2B9, A4B9, and A6B9 cases to represent a range of wind shear magnitudes. As expected, the impact of the large eddies in the fully 3D no-fire simulations was to mix the stronger momentum in the upper half of the mixed layer to the surface. For example, turbulent mixing in the strong shear A2B9 case contributed to an increase in the surface wind speed (decrease in B), such that the wind profile and 2D convective regime were nearly identical to the weak shear A6B9 case. The boundary layer experiments thus suggest that although some cases feature wind profiles uncharacteristic of a well-mixed boundary layer, the parameter space covers a range of well-mixed wind profiles. Findings in this study thus have broad relevance because the parameter space examined depicts a range of background conditions, from well-mixed boundary layers to strong shear profiles characteristic of, for example, frontal passages or jets aloft (keeping in mind, however, that $N^2 \approx 0$ s^{-2} in these experiments).

It is important to note that because the parcel heating process is independent of surface wind direction, two cases may have the same U_s but different surface wind direction. Furthermore, cases can have identical values of $\bar{U}$ and U_s, but one wind profile will contain a reversal of wind direction at some height above the surface whereas the other will consist of uniform wind direction with height (Fig. 1c). Two pairs of simulations (A4B6 and A4B5) in the matrix have this issue. Although the A4B5 and A4B6 cases are the only A/B combinations in the matrix with two simulations, several other cases exhibit wind reversals, mainly in the upper right portion of the matrix. The implications of a wind reversal for plume behavior will be discussed in section 4b.

4. Results and discussion

a. Organizational modes

Upon completion of all 56 cases in the $\bar{U} - U_s$ experiment matrix, organizational modes were diagnosed subjectively by first identifying benchmark cases for the multicell and intense plume modes based on the regime definitions outlined in section 1 and then classifying the remaining 54 cases based primarily on vertical cross sections and Hovmöller diagrams of vertical velocity. Time series of domain maximum vertical velocity $w_{\max}$ and domain-averaged upward mass flux $\overline{M}$ were also examined to corroborate the other analyses and further subdivide the modes. It is worth noting that this combination of statistics includes a local measure of updraft strength ($w_{\max}$) and a measure of the gross behavior of updrafts across the domain ($\overline{M}$).

The analysis reveals that the multicell mode is separated into two subclasses: strong and weak. Figure 2 presents (left) vertical cross sections and (right) Hovmöller diagrams of vertical velocity for each of the modes diagnosed. Updrafts in strong multicell cases grow vertically such that they extend through the depth of the mixed layer, whereas updrafts in weak multicell cases are unable to deepen beyond the lowest 1/3 to 1/2 of the mixed layer (cf. Figs. 2c,d). Maximum updraft vertical velocities are generally 5–10 m s^{-1} greater and domain-averaged upward mass fluxes are typically 0.25–0.75 kg m^{-2} s^{-1} greater for the strong compared to the weak multicell cases. This distinction is potentially quite important because deep cells are capable of mixing air with high momentum and low relative humidity from

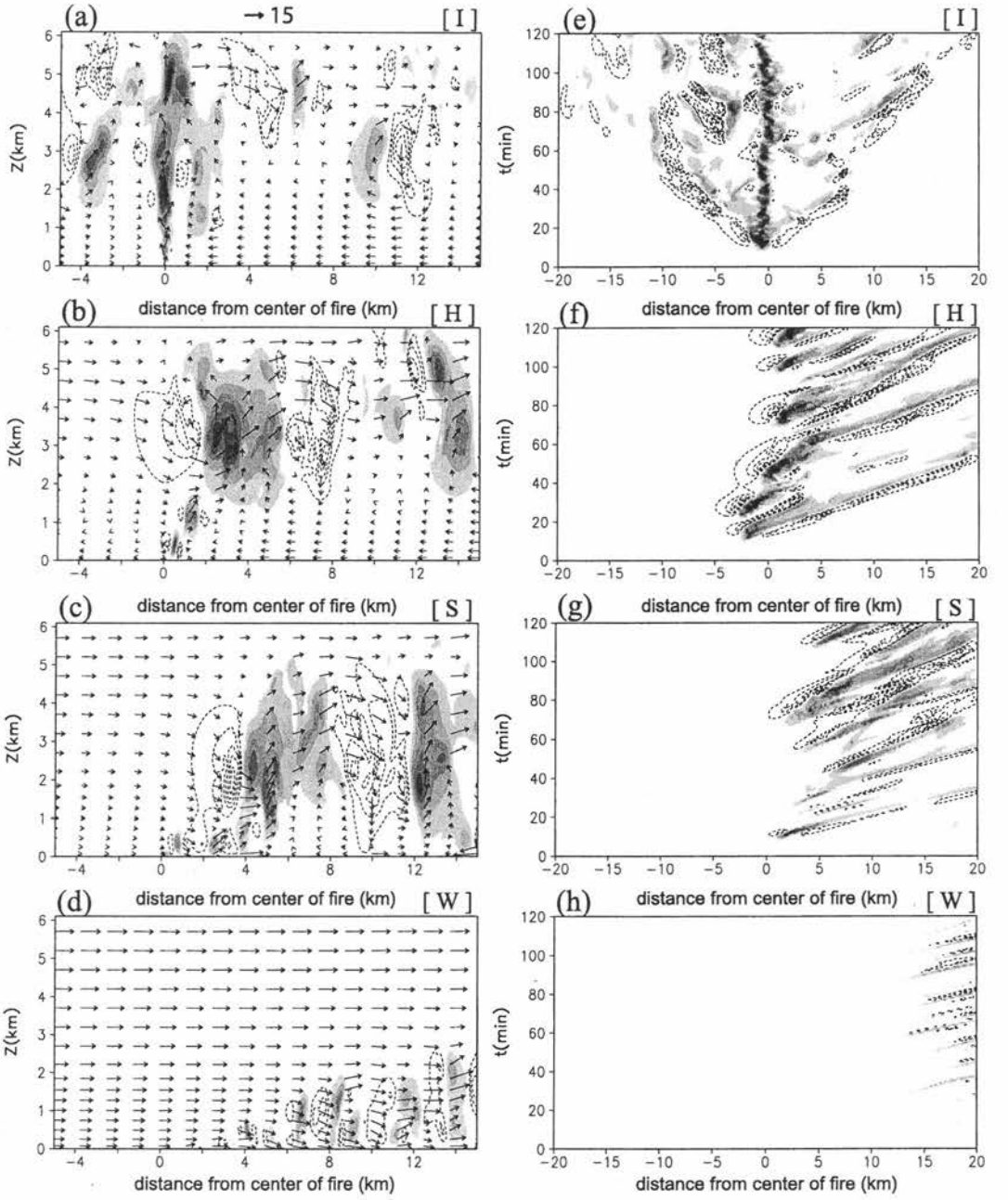

FIG. 2. Examples of organizational modes: (a),(e) Intense plume (A1B8), (b),(f) hybrid (A3B5), (c),(g) strong multicell (A4B9), and (d),(h) weak multicell (A6B3). Mode classification is indicated above each panel: I, intense plume; H, hybrid; S, strong multicell; W, weak multicell. Left panels are vertical cross sections of vertical velocity (positive: shaded, negative: dashed contour; m s^{-1}) and total wind vectors (m s^{-1}); right panels are Hovmöller diagrams of vertical velocity at $z = 3$ km. All figures are in a frame of reference moving with the fire.

the free atmosphere to the surface where erratic fire behavior may occur, similar to what is described by Charney and Keyser (2003). Updrafts in strong multicell cases are also better able to loft firebrands (flaming or smoldering material such as leaves and/or pinecones) to higher altitudes than their weak counterparts and are generally warmer, leading to slower extinguishing rates. However, the potential for spotting (fire ignition isolated from main fire) may be greater for the weak multicell mode because firebrands are less likely to extinguish before reaching adjacent fuels if they exit updrafts closer to the surface (Albini 1983).

A hybrid classification is also defined for cases that do not fit completely within the intense plume or multicell modes. In this class, upward motion is contained within a vertical column, similar to the intense plume mode, but the upward motion takes the form of discrete cells, similar to the multicell mode (Fig. 2b). In terms of potential impact on a wildfire, the primary difference between the hybrid mode and the intense plume mode is the more unsteady nature of the hybrid mode. Whereas the intense plume mode can tap into the free atmosphere and loft firebrands high in the mixed layer nearly continuously, the hybrid mode cases exhibit periods of time when convection is weak and shallow.

The complete set of mode classifications is presented in Fig. 3. Intense plume and hybrid mode cases are found within the $A < 1$ half of the parameter space, with multicell convection the dominant mode for $A > 1$. Thus, a critical value of mean wind exists such that a weaker mean wind speed supports a single deep plume (and no new convection near the fire) and a stronger mean wind speed results in periodic regeneration of convection downstream of the fire. Within the high-advection (i.e., $A > 1$) area of the parameter space, strong (weak) multicell classifications are more common for $B > 1$ ($B < 1$). This strongly suggests that the fundamental process controlling the depth and magnitude of multicell convection is parcel heating. The basic processes encapsulated in the two control parameters will be discussed in the sections that follow. The predominance of overturning wind profiles in the hybrid area of the parameter space, a conspicuous feature of the classification, will be addressed later when considering the low-advection area of the parameter space.

b. *Parcel heating process*

1) HIGH MIXED LAYER ADVECTION ($A > 1$) CASES

The sensitivity of convection to surface parcel buoyancy is obtained by comparing time series of $w_{\max}$ and $\overline{M}$ for four cases, each representing a different area of the B parameter space (Fig. 4). For both A5 and A6 cases, updrafts in the strong multicell regimes ($B > 1$) exhibit a $w_{\max}$ 3–6 m s^{-1} greater than the weak multicell cases ($B < 1$) for virtually the entire time period, with analogous results for $\overline{M}$. Although substantial variability is clearly evident for each case and brief periods of time exist in which the highest B case does not exhibit the largest values of $w_{\max}$ or $\overline{M}$, a signal of increasing updraft strength with increasing B is present. This is supported by a comparison of time-averaged $w_{\max}$ and $\overline{M}$ (Table 1).

Hovmöller diagrams of $z = 3$ km vertical velocity for the A5B9 and A6B9 cases (Fig. 5) show that strong multicells first reach the Hovmöller plane approximately 5 km downstream of the surface heating, similar to the strong multicell example in Fig. 2. To reveal the transient processes that yield strong multicells in the A5B9 case and to explain why convection in that case remains relatively shallow within 5 km of the heat source, a massless air parcel was introduced at the lowest model level ($z = 1.25$ m) at $x = 20$ km (center of fire) every 4 min (three parcels total, denoted hereafter by a ○, △, or □). The 4-min averaged fields of vertical velocity in Fig. 6 indicate that parcels exhibit two primary episodes of ascent, the first within 2–3 km of the heat source, associated with the rapid development of shallow cells (denoted by S), and the second 4–6 km downstream of the heat source, associated with the more gradual development of deep cells (denoted by D). At each time, the parcels ascend up to about 1 km AGL and then experience downward acceleration and descent before either accelerating upward into the deep cell (○ and △) or moving laterally through the top of the cell (□). The behavior of the three parcels is consistent with the merging of cells S2 (cell associated with □) and S1 (cell associated with ○ and △) in Fig. 6d into the deep cell D2 in Fig. 6e. Note that because individual air parcels move independently of the updraft cells, a parcel may outrun an updraft, as in parcel △ in Fig. 6d, and vice versa.

Because the parcels do not rise continually after heating from the fire, and because in some cases they are accelerated downward despite their positive buoyancy, the perturbation pressure gradient is of primary importance. To analyze the perturbation pressure field, it is helpful to consider the diagnostic pressure equation

$$\nabla^2 p' = -\nabla \bullet [\rho_o(\mathbf{u} \bullet \nabla)\mathbf{u}] + \frac{\partial}{\partial z}(\rho_o B), \qquad (4)$$

and to decompose Eq. (4) (as in Rotunno and Klemp 1982) into buoyant and dynamic components ($p' = p'_B + p'_D$) for a 2D flow, which yields

$$\nabla^2 p'_B = \frac{\partial}{\partial z}(\rho_o B) \quad \text{and} \qquad (5)$$

$$\nabla^2 p'_D = -\rho_o\left[\left(\frac{\partial u}{\partial x}\right)^2 + \left(\frac{\partial w}{\partial z}\right)^2\right] - 2\rho_o\left(\frac{\partial u}{\partial z}\frac{\partial w}{\partial x}\right), \qquad (6)$$

where $B = -(\rho'/\rho_o g)$ and all other variables have their conventional meanings. The linear part of Eq. (6) may be written as

$$\nabla^2 p'_{DL} = -2\rho_o\left(\frac{\partial U}{\partial z}\frac{\partial w}{\partial x}\right), \qquad (7)$$

	U_s	0	1.25	2.5	3.75	6.25	7.5	8.75	10.0	12.5
$\overline{U}$	A B	∞	3.4	1.7	1.1	0.7	0.6	0.5	0.4	0.3
0	0	A1B9	A1B8	A1B7	A1B6	**A1B5**	**A1B4**	**A1B3**	**A1B2**	**A1B1**
2.5	0.3	A2B9	A2B8	A2B7	**A2B6**	**A2B5**	**A2B4**	**A2B3**	**A2B2**	**A2B1**
3.75	0.6	A3B9	A3B8	**A3B7**	A3B6	**A3B5**	**A3B4**	**A3B3**	**A3B2**	**A3B1**
6.25	1.7	A4B9	A4B8	A4B7	A4B6	A4B5	A4B4	A4B3	A4B2	A4B1
10	4.3	A5B9	A5B8	A5B7	A5B6	A5B5	A5B4	A5B3	A5B2	A5B1
12.5	6.8	A6B9	A6B8	A6B7	A6B6	A6B5	A6B4	A6B3	A6B2	A6B1

FIG. 3. Matrix of control parameter experiments, with organizational mode overlaid. Multicell cases are shaded dark (strong multicell) and light (weak multicell), with intense plume cases unshaded and hybrid cases outlined with a dashed line. Cases with base state bulk Richardson number less than or equal to 0.25 are indicated by bold text and cases with base state wind reversal profiles indicated by underlined text.

where the horizontal wind speed u has been decomposed as $u(x, z, t) = U(z) + u'(x, z, t)$. This is the part of the dynamic pressure associated with an updraft's presence in a sheared base state environment. The remaining nonlinear dynamic contributions are due to interactions with the locally perturbed flow. Equation (5) therefore indicates that a perturbation pressure maximum (minimum) is expected where buoyancy decreases (increases) with height, and Eq. (7) dictates that a pressure maximum (minimum) is expected upshear (downshear) of an updraft. Any other dynamical effects are encompassed in the nonlinear part of the dynamic perturbation pressure component p'_{DNL}, where DNL is the nonlinear dynamic component. For a more complete discussion of the various dynamic pressure components, the reader is referred to Klemp (1987) and his application of the procedure to the dynamics of tornadic thunderstorms.

Using the above pressure decomposition, the irrotational equation of motion can be written as

$$\underbrace{\frac{D\mathbf{u}}{Dt}}_{\text{ACC}} = \underbrace{-\frac{1}{\rho_o}\nabla p'_B - \underbrace{\mathbf{g}\left(\frac{\rho'}{\rho_o}\right)}_{\text{BUOY}}}_{\text{ACCB}} \underbrace{-\underbrace{\frac{1}{\rho_o}\nabla p'_{DL}}_{\text{ACCDL}} - \underbrace{\frac{\rho'}{\rho_o}\nabla p'_{DNL}}_{\text{ACCDNL}}}_{\text{ACCD}}. \tag{8}$$

Examining the decomposed pressure fields in Fig. 7, it is apparent that total buoyant acceleration (ACCB) is approximately zero between $z = 750$ and 1000 m. This weak total buoyant acceleration field is due to a combination of entrainment, reducing parcel buoyancy, and a downward directed buoyant pressure gradient force. As a result of the weakly positive ACCB, parcels respond to local pressure perturbations near the top of the shallow cell layer and are accelerated downward (ACCD; see ACCD vectors in Fig. 7c). The shallow cells then move downstream with little vertical development until approximately $t = 76$ s when deep convection develops (cf. Figs. 6d,e).

The development of the shallow cells is initiated by the surface heating, as suggested by the field of strong buoyancy and minimal amount of dynamic forcing for ascent in the left panels of Fig. 7. Between $t = 60$ and $t = 77$ min, cell S1 moves downstream (later joined by S2) with only modest changes in intensity and depth. Cell D1, centered about 6 km downstream of the fire in 6a, having formed shortly prior to the analysis time, is apparently cut off from the source of buoyancy by $t =$ 60–64 min (see Fig. 7a). The cell translates downstream, reaching a maximum in intensity about 10 km downstream of the heat source before gradually weakening (Fig. 5a). The ACCB and ACCD fields on the upstream side of D1 in Fig. 7 are approximately equal in magnitude and contribute to upward acceleration. Comparing Figs. 7c and 7d, it is apparent that ACCDNL is the dominant component of ACCD, with weak ACCDL directed downward due to a local p'_{DL} maximum above the D1 inflow.

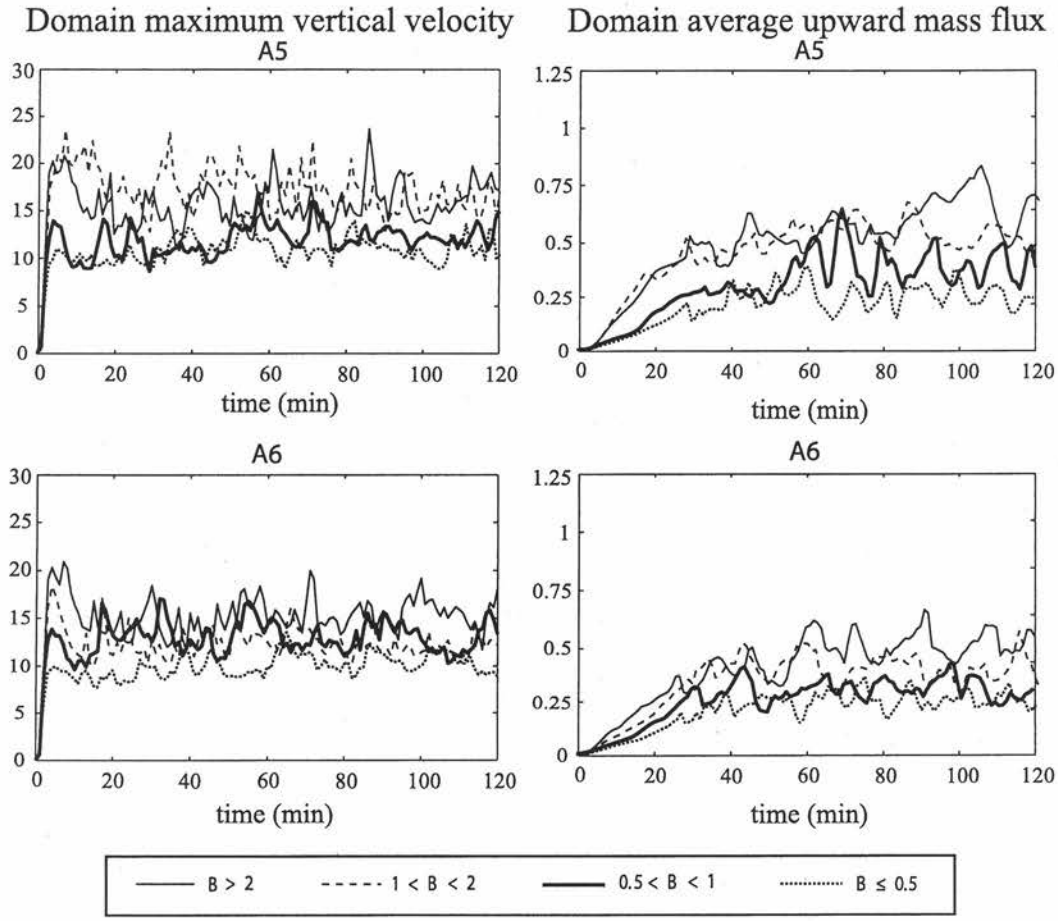

FIG. 4. (left) Time series of domain maximum plume vertical velocity (w_{max}; m s^{-1}); (right) Domain-averaged upward mass flux ($\overline{M}$; kg m^{-2} s^{-1}). A5 (A6) cases displayed in upper (lower) panels. See Table 1 for temporally averaged (t = 40–120 min) values.

The averaging procedure masks the process of shallow cell splits and mergers that occurs within 4–6 km of the heat source between 60–76 min. Figure 8 illustrates the series of cell interactions that occur between $t = 71$ and $t = 76$ min. A similar process of cell splitting and merging was described in Kiefer et al. (2008); however, the less intense surface heat source in that study yielded only the weak multicell mode. The final panel of Fig. 8 occurs immediately following formation of the deep cell (D2). In the time-averaged field in Fig. 6, the final cell merger occurs between Figs. 6d and 6e. As mentioned earlier, the behavior of parcel □ is consistent with the merging of cells S1 and S2 to form D2 because cell S2 (with which □ is associated) forms the upper part of D2. As cell D2 moves downstream between Figs. 6e and 7f, a new shallow cell (S3) forms just downwind of the fire, completing the cycle begun in Fig. 6a. Figure 8 suggests that the presence of substantial base state wind shear may be important for the deep cell development because cell speed is height-dependent, leading to cells becoming sheared apart (splitting) or superimposed (merging). It is noteworthy that for the cases with no base state wind shear, intense plumes transition to weak multicells with increasing mean wind speed. However, the strong multicell class is not simulated.

The aperiodicity and highly variable location of deep cell development in Fig. 5a is consistent with the series of nonlinear splits and mergers that ultimately leads to

TABLE 1. Temporally averaged values of domain maximum vertical velocity w_{max} (m s^{-1}) and domain averaged upward mass flux $\overline{M}$ (kg m^{-2} s^{-1}) for select cases within the A5 and A6 rows of the experiment matrix. Elements in table are in format $w_{max}/\overline{M}$. Averaging is performed between t = 40 min and t = 120 min.

	$B > 2$	$1 < B < 2$	$0.5 < B < 1$	$B \leq 0.5$
A5	15.9/0.6	17.1/0.6	12.6/0.4	11.3/0.3
A6	15.1/0.5	13.3/0.4	13.0/0.3	11.0/0.2

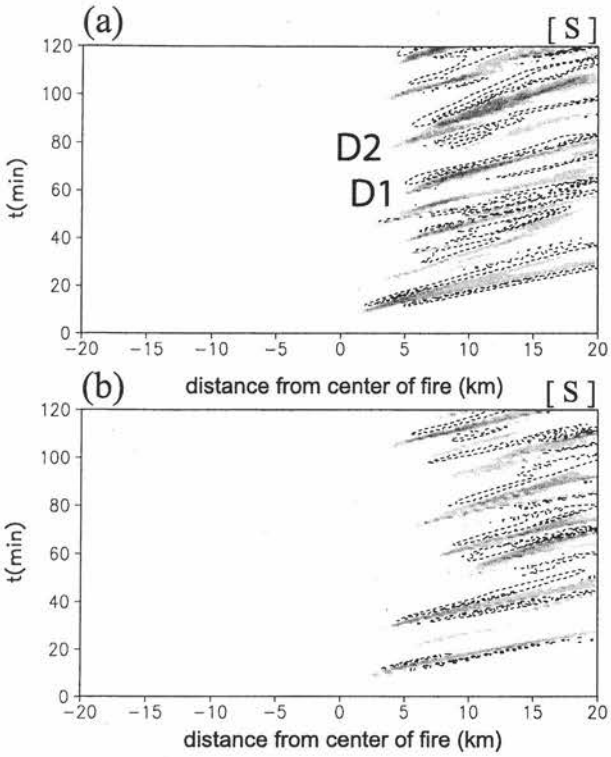

FIG. 5. Hovmöller diagrams (positive: shaded, negative: dashed contour; m s^{-1}) of vertical velocity at $z = 3$ km, for the (a) A5B9 and (b) A6B9 cases. Cells near $t = 60$ min and $t = 80$ min in (a) are labeled D1 and D2, respectively (see text). Mode classification as in Fig. 2. All figures are in a frame of reference moving with the fire.

deep cell development. Although the position (with respect to the fire) and timing of deep cells is not deterministic, the likelihood of deep cell development is predictable, given knowledge of the B parameter. With decreasing B parameter, initial shallow cells become weaker and the buoyant and dynamic forcing similarly weaken to the point that only weak vertical development of updrafts occurs within 4–6 km of the downstream edge of the heat source [e.g., A5B2 ($B < 0.5$) case, not shown]. Cell tops in the weak multicell mode may reach as high as 3–4 km, but cells do not reach such depths until 10 km or more from the fire. Although a universal "realm of influence" for a dry convective cell is unlikely to exist, a rough approximation can be attained by considering the ways in which a cell can impact its environment. Turbulent mixing effects are local in nature, and gravity waves, capable of impacting the atmosphere on the mesoscale, are unlikely to propagate upstream (toward the fire) with nearly dry adiabatic lapse rates and strong advection. The elimination of turbulence and gravity waves leaves perturbation pressure fields induced by convection, capable of producing dramatic changes to the wind field. Scale analysis (not shown) indicates that perturbation pressure fields should be of the same scale as the convection. This suggests that if a cell with scale O(1 km) deepens and/or intensifies at a distance O(10 km) from a fire, its impact on the atmosphere near the fire should be minimal.

2) LOW MIXED LAYER ADVECTION ($A < 1$) CASES

Attention is now directed to the area of the parameter space where advection by the mean wind is weak ($A < 1$). Figure 9 indicates that until approximately $t = 15$ min, w_{max} is greater for high-buoyancy cases than for low-buoyancy ones. However, after $t = 15$ min, the low-A cases do not exhibit increasing w_{max} (or $\overline{M}$) with increasing B. The low-B cases are generally at least as strong as the high-B cases and in fact are at times substantially stronger than the high-B cases. This anomalous behavior is most pronounced for the A2 group during the last 50 min of simulation and is apparent in both the w_{max} and $\overline{M}$ time series as well as in temporally averaged values (Table 2). Forcing for parcel ascent was again examined, although in this case the focus was not on the transient nature of the forcing but on the source regions for air parcels involved in the strong convective motions. What is of interest in this analysis is not the high-frequency variability (evident in Fig. 9 as changes in w_{max} over periods of 5–10 min) but the overall strength of the plume in the A2B2 case and why the statistics do not conform to our expectations based on the B parameter.

A unique aspect of the cases in the low-A, low-B area of the parameter space is the overturning nature of the wind profile. Figure 10a depicts a subset of trajectories of 18 parcels released in the A2B2 case (9 low level, 9 upper level) and indicates that in addition to the source of low-level parcels moving from right to left in the domain, a substantial number of air parcels moving from left to right in the upper 1 km of the mixed layer descend to within a few hundred meters of the surface and eventually transit through the core of the plume. Analysis during the first hour of the simulation (not shown) indicates that the downdraft just upshear of the plume (Fig. 10a) develops as a result of air parcels traversing a region of downward-directed pressure gradient forcing at and below the mixed layer top. A layer of positive perturbation pressure, associated with a strong gradient of buoyancy just above the mixed layer (due to adiabatic cooling at plume top), results in the downward-directed pressure gradient force. The parcel trajectories within and adjacent to the downdraft are quite similar to streamline analyses derived from Doppler lidar data from the mature stage of the 1988 Battersby Township fire detailed in Banta et al. (1992). Further comparison to the real world case is strongly limited by the absence

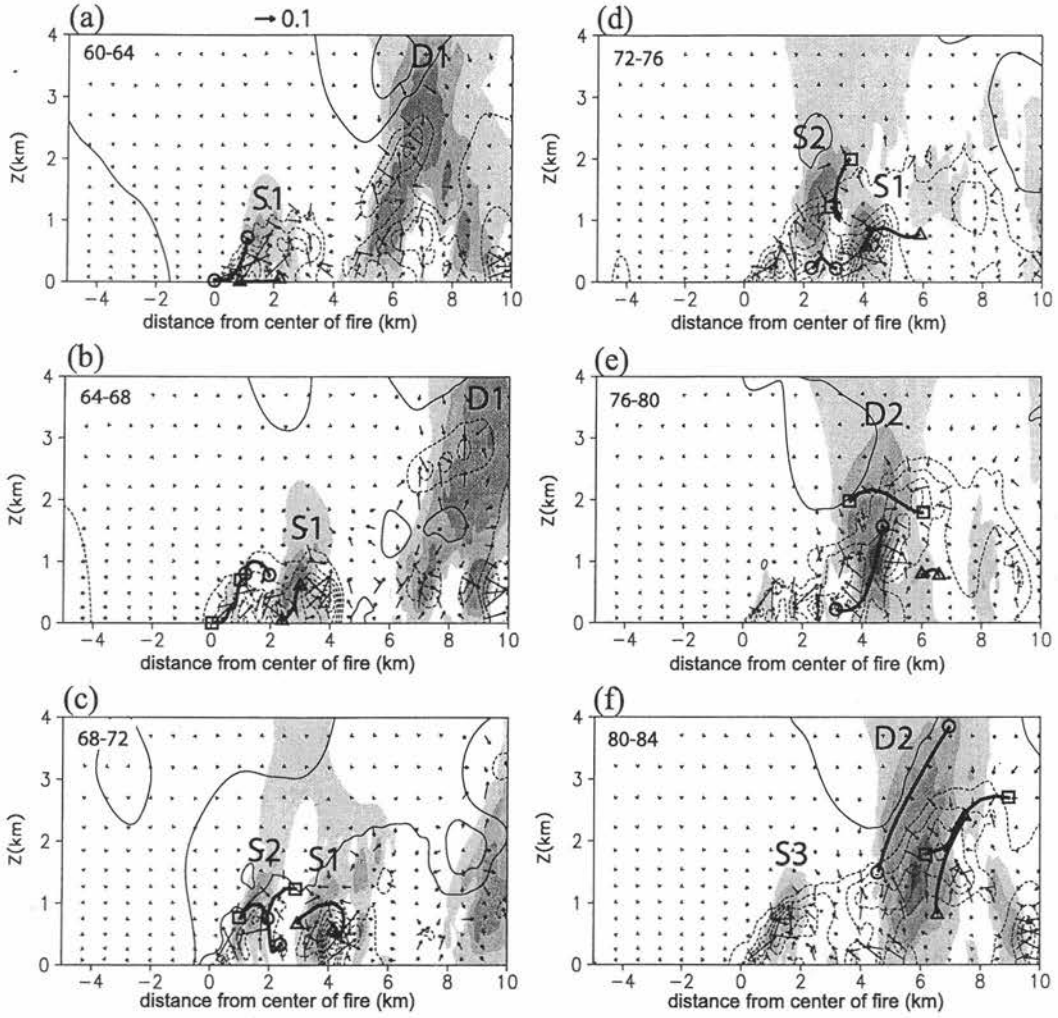

FIG. 6. Mean vertical velocity (shaded; m s^{-1}), perturbation pressure (contoured; Pa), and acceleration vectors (m s^{-2}) for simulation A5B9. Fields are averaged in 4-min increments between 60 and 84 min, with averaging periods of (a) 60–64, (b) 64–68, (c) 68–72, (d) 72–76, (e) 76–80, and (f) 80–84 min displayed. Shading increment is 2 m s^{-1} and contour interval is 20 Pa. Cells are labeled *S* (shallow) and *D* (deep); numbering refers to order of development. All figures are in a frame of reference moving with the fire.

of moist convective processes in this study. However, a similar feature was detailed by Palmer (1981) in analyses of large fires where moist convection was not observed. Also of interest in Fig. 10a are the parcels in the inflow layer above about 750 m that overturn and in some cases descend and return to the inflow layer. The fact that air parcels such as □ accelerate into the updraft and yet never come into contact with low-level heating motivates further analysis.

The 4-min averaged fields of vertical velocity and perturbation pressure in Fig. 11 depict a quasi-steady plume, with a gradually broadening area of moderate vertical velocity on the downshear (right) side. Of interest is the fact that the surface air parcel (○) and upper-level air parcel (△) follow similar trajectories and experience comparable accelerations once in the plume, despite their disparate origins (see Fig. 11). For parcel ○, decomposed local acceleration vectors for the averaging period 98–102 s (Fig. 12, left) suggest a large contribution from ACCB, in spite of the downward-directed pressure gradient force associated with the buoyancy field (i.e., p'_B term). By the time the upper-level parcel (△) is ascending through the plume (Fig. 12, right), nonzero deep layer advection ($A > 0$) has shifted the plume toward the fire such that the plume is directly above the heat source and buoyancy extends through a deeper layer than during the previous averaging period. ACCB, with some contribution from ACCDNL, drives the ascent of parcel △ through the plume. Of great interest here is that a parcel need not originate in the layer

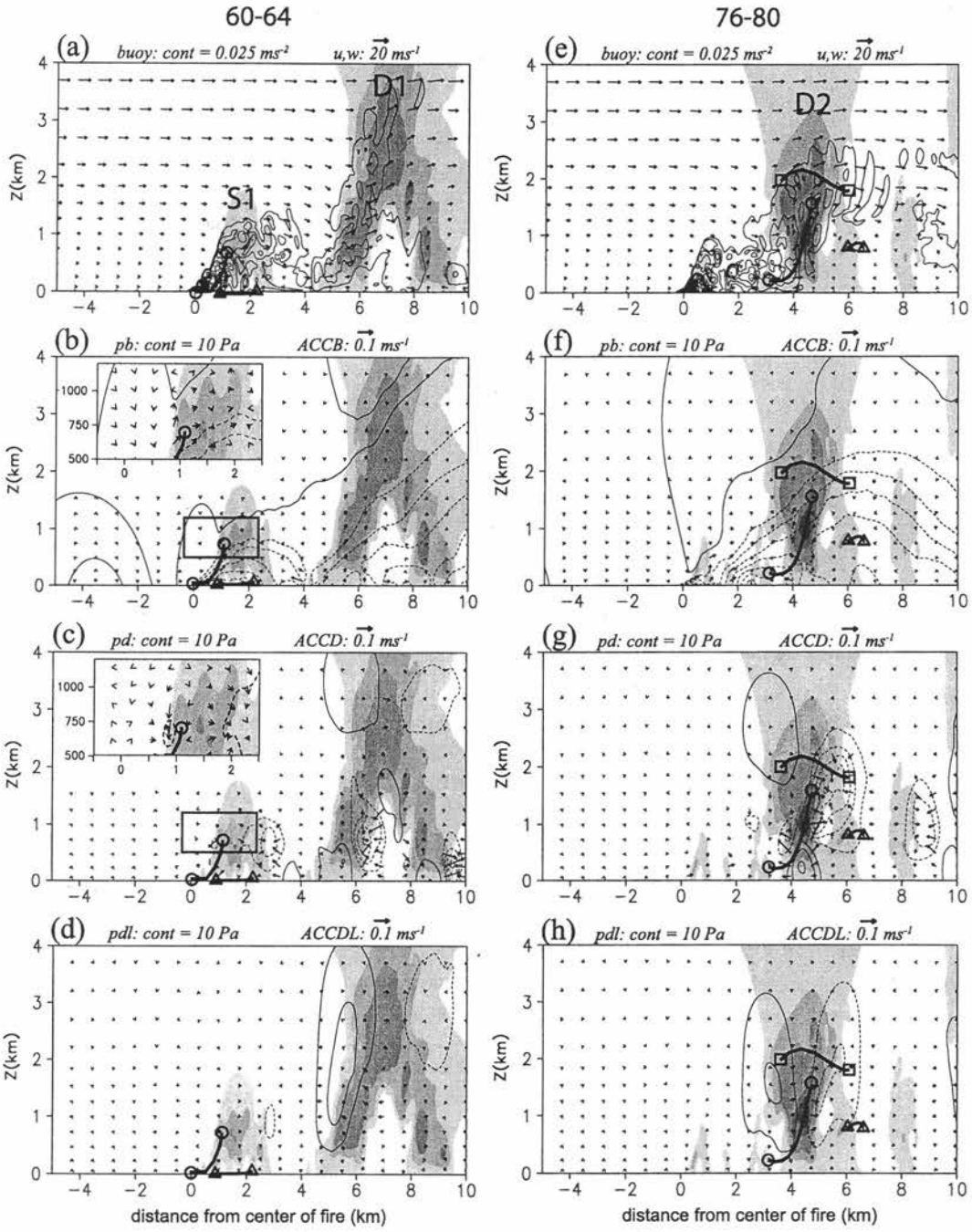

FIG. 7. Mean fields of (a),(e) buoyancy (BUOY), (b),(f) buoyant pressure perturbation component (Pb), (c),(g) dynamic pressure perturbation component (Pd), and (d),(h) linear dynamic pressure perturbation component (Pdl) for two averaging periods, (a)–(d) 60–64 min and (e)–(h) 76–80 min, for simulation A5B9. Vectors depicted include (a),(e) total wind field, (b),(f) ACCB, (c),(g) ACCD, and (d),(h) ACCDL; (a) and (c) contain inset figures, with an outline of the inset region displayed in each panel. Mean vertical velocity is shaded with 2 m s^{-1} increments for all panels (including inset figures). Contour intervals and vector scales are shown for each panel and vary among (a)–(h). Cells are labeled as in Fig. 6. All figures are in a frame of reference moving with the fire.

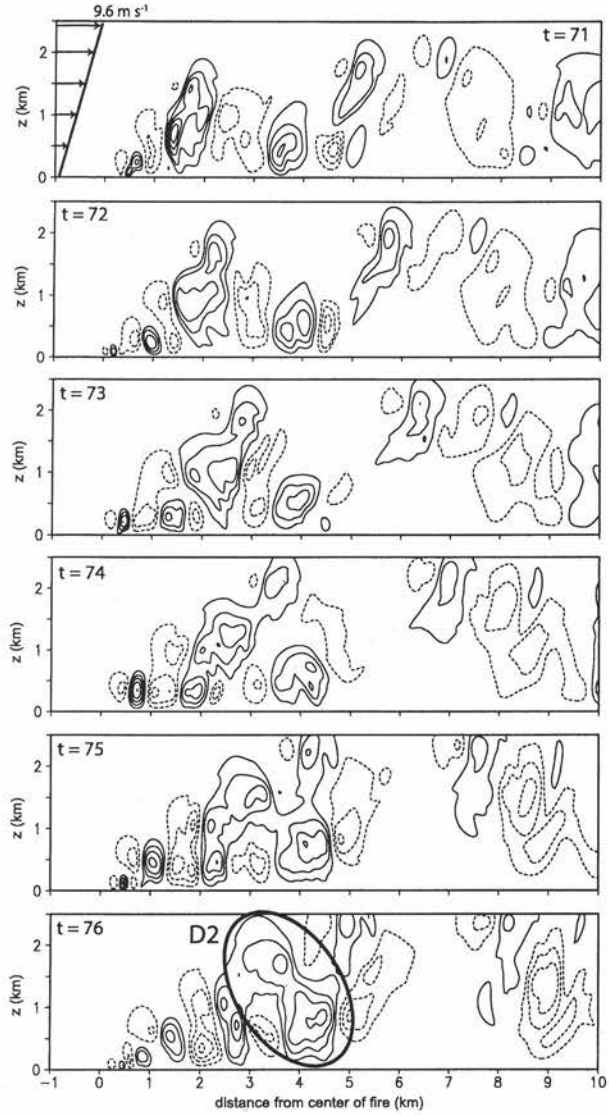

FIG. 8. Vertical cross sections of vertical velocity for the A5B9 case, at 1-min intervals between $t = 71$ and $t = 76$ min. Contour interval is 3 m s^{-1}; positive (negative) values contoured with solid (dashed) line. Cell D2 labeled in bottom panel. Base state wind profile included in top panel, with wind speed at top of cross section indicated. All figures are in a frame of reference moving with the fire.

of near-surface inflow to contribute to the strength of the plume. This is a unique feature of the low-A, low-B area of the parameter space because the base state wind profile yields two streams of air parcels directed toward the buoyant plume. The additional source of upper-level air parcels is not accounted for in the simple model of plume generation and is a possible factor in the plume statistics not conforming to our expectations.

The parcel initialized upstream of the plume at $z = 1$ km (□) moves beneath a pressure minimum located near $x = +4$ km, $z = 2.75$ km at $t = 110$ min (Fig. 11d) and subsequently accelerates upward into a broad region of modest vertical velocity (Fig. 11e). It is apparent from Fig. 10a, however, that parcels in the 500–1000-m layer that move beneath the p' minimum also ascend into the updraft core. An examination of the decomposed pressure fields for the A2B2 case (Fig. 12) reveals that the source of the pressure minimum is dynamic, partly because of the sheared basic wind profile (p'_{DL}term) and partly because of a small transient circulation immediately downshear of the plume (p'_{DNL}term). This local gyre initially developed along the horizontal gradient of buoyancy on the downshear edge of the plume (not shown). The gyre remains adjacent to the plume for approximately 10 min before moving downshear, away from the plume. Although the p'_{DNL} term contribution is significant over relatively short time periods, it is the p'_{DL} term that contributes to plume behavior over the broader time period of interest in this analysis. The forcing of air parcels within the 500–1000-m layer by the downshear pressure minimum is partially accounted for by the control parameters because $w_{\max}$ influences the perturbation pressure field through the $\partial w/\partial x$ component of Eq. (6). However, the sheared base state is unaccounted for by either of the control parameters and is an additional source for the unexpected $w_{\max}$ and $\overline{M}$ in Fig. 9, in addition to the source of parcels from the top of the mixed layer, as just discussed.

In contrast to the A2B2 case, parcels that ascend through the plume in the A2B9 case can be traced back to one region: the lowest 500 m above the heat source. This can be seen in Figs. 10 and 13, where a parcel traversing the heat source at the surface eventually grazes the right edge of the plume and a parcel crossing the heating at $z = 500$ m ascends along the left edge of the plume. The layer of air parcels above the fire ascends into the plume in a smooth and ordered fashion, in contrast to the more chaotic nature of parcel trajectories in the A5B9 (strong multicell) case. The very shallow layer of buoyant air (Figs. 14a,e) and the resulting strong vertical gradient of p'_B (Figs. 14b,f) appear to nearly balance, strongly limiting vertical movement of near-surface air parcels downstream of the heat source. The key factor for parcel upward acceleration appears to be the movement of air parcels away from the strong near-surface buoyant pressure gradient, best seen in a pressure decomposition analysis focused on the plume (Fig. 15). Above about 500 m, ACCB and ACCDNL drive upward parcel motion, with ACCDNL being the larger component. The large importance of ACCDNL is consistent with the steady nature of the plume; perturbations from the base state wind field are long-duration phenomena and play a fundamental

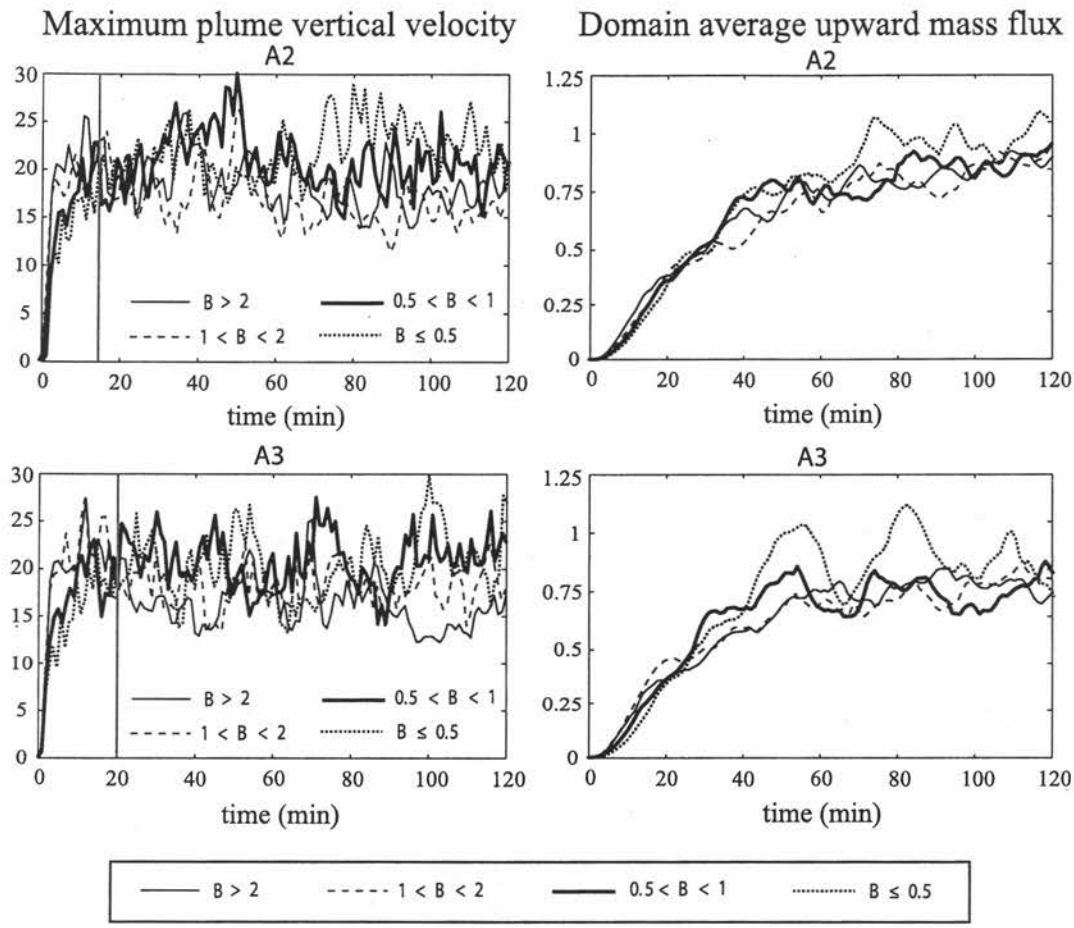

FIG. 9. As in Fig. 4 but for (top) A2 and (bottom) A3 cases. Vertical line in left panels marks end of initial period when w_{max} increases with increasing buoyancy parameter (B); see text for details. See Table 2 for temporally averaged (t = 40–120 min) values.

dynamical role in forcing vertical motion in the intense plume case. The balance of $-1/\rho_o \partial p'_b/\partial z$ and BUOY evident in Figs. 15b,e is indicative of hydrostatic balance, an aspect that is at first unexpected but is not unreasonable considering the steady nature of the surface heating and flow over the heating.

c. *Mixed layer advection process*

It is apparent from comparison of vertical cross sections of the strong multicell (e.g., Fig. 6) and intense plume (e.g., Fig. 13) cases that convective cells develop closer to the heat source as the mean wind increases. For the A2B9 case (intense plume), a shallow layer of warm air extends several kilometers downwind of the heat source, beyond which cells form, deepen, and merge into the intense plume (not shown). When averaged over several minutes, the vertical velocity cross section consists of a tilted, continuous updraft at the downstream edge of the shallow warm layer (Figs. 14a,e or 15a,d). For the A5B9 case (strong multicell), no downstream shallow layer of warm air exists. Shallow cells form adjacent to the heat source and move downstream while undergoing a period of splitting and merging (Fig. 8). Several kilometers downstream of the heat source, a number of small cells merge into one large cell that then deepens while moving downstream. The process then begins again as new shallow cells form downstream of the fire (Figs. 6d–f). The A3B9 and A4B9 cases, straddling the intense plume/strong multicell boundary, are transitional cases. The A3B9 case does not feature a continuous region of shallow warm air downstream of the fire; instead, it features small (<1 km

TABLE 2. As in Table 1, but for cases within the A2 and A3 rows of the experiment matrix.

	$B > 2$	$1 < B < 2$	$0.5 < B < 1$	$B \leq 0.5$
A2	17.9/0.8	17.0/0.8	20.8/0.8	22.3/0.9
A3	15.9/0.7	18.0/0.7	21.0/0.7	21.0/0.9

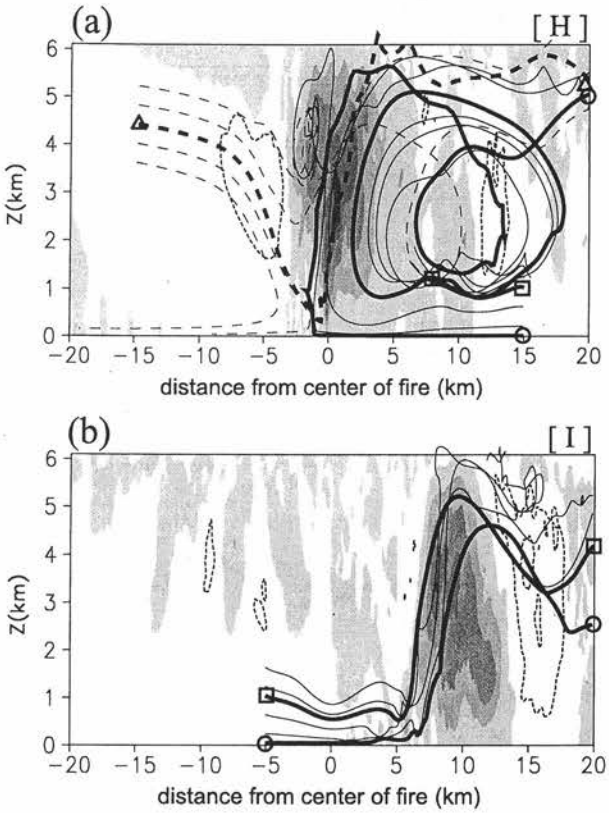

FIG. 10. Mean vertical velocity (positive: shaded, negative: short dashed contour; contoured every 3 m s^{-1}) for cases (a) A2B2 and (b) A2B9. Trajectories of air parcels released 15 km upstream of the mean plume position displayed (solid: low level; dashed: upper level); thick contours and symbols indicate parcel trajectories discussed in text. Note that not all parcel trajectories are displayed in figure. Averaging is from 80 to 120 s. Mode classification as in Fig. 2. All figures are in a frame of reference moving with the fire.

deep) cells that form immediately downstream of the heating, propagate downstream for several kilometers, and merge into the intense plume (not shown). The A4B9 case closely resembles the A5B9 case in terms of cell behavior (not shown).

An interesting feature consistent with the above behavior is the development of quasi-steady positive u' near the surface in the intense plume cases but not in the strong multicell cases (Fig. 16). The u' field is not entirely associated with inflow into the plumes, however; strong, steady perturbations are maintained in the vicinity of the heat source even as the plume moves 5–10 km downstream (e.g., A2B9 case in Fig. 16). The perturbations originate at the position of the heat source and spread both upstream and downstream of the fire, with the speed of the upstream perturbation front decreasing with increasing mean wind. This behavior is consistent with that of a buoyancy bore (e.g., Mapes 1993), permanently altering the near-surface wind speed as it passes a given point with phase speed N/m, where N is the Brunt–Väisällä frequency and m is vertical wavelength. As wind speed increases further, no upstream movement is evident and only the streaks of u' associated with multicells are present.

Of great importance is the steady, strong u' over and downstream of the heat source in the low-A cases. The near-surface advection is actually stronger in the low-A cases than the high-A cases as a result of the passage of the borelike feature. The aforementioned hydrostatic layer downstream of the fire in the A2B9 case is associated with this strong near-surface advection. As the deep cell that forms shortly after model startup (prior to the bore) is slowly advected by the weak mean wind away from the heat source, some combination of inflow into the cell and the permanent u-wind perturbation rapidly advect heated air downstream. The pressure gradient force resulting from the strong vertical gradient of buoyancy approximately balances BUOY for several kilometers downstream of the heating, as a result of the strong, steady advection. The magnitude of the u-wind perturbation downstream of the heat source is smaller in the A3B9 case, resulting in weaker advection (leading to a weaker vertical gradient of buoyancy and perturbation pressure) and stronger parcel heating. The combination of these two effects yields cell formation closer to the heating. A further increase in mean wind speed results in a full transition to the strong multicell mode.

A series of additional experiments were performed to examine how an adjustment to static stability (and therefore linear phase speed) would affect cases near the plume/multicell border (i.e., cases A3B9 and A4B9). In an experiment with a statically stable ($N = 0.007\ \mathrm{s}^{-1}$) base state thermal profile, the A4B9 case exhibited an upstream propagating bore (not shown), similar to the weak advection cases in Fig. 16. Associated with the steady flow over the heat source was a shallow layer of warm air downstream of the heat source and a single deep updraft, consistent with the intense plume mode. A similar experiment, with a statically neutral ($N = 0\ \mathrm{s}^{-1}$) base state thermal profile applied to the A3B9 case, resulted in a shift from intense plume to strong multicell. Further examination of the apparent bore feature and its impact on organizational mode is left to future work.

The analysis now proceeds to examination of $w_{\max}$ and $\overline{M}$ time series with a constant B parameter. Statistics from the high- and low-buoyancy areas of the parameter space will be examined to better understand the impact of mixed layer advection on the intensity of convection. The discussion will then conclude with an analysis of the relationship between advection and

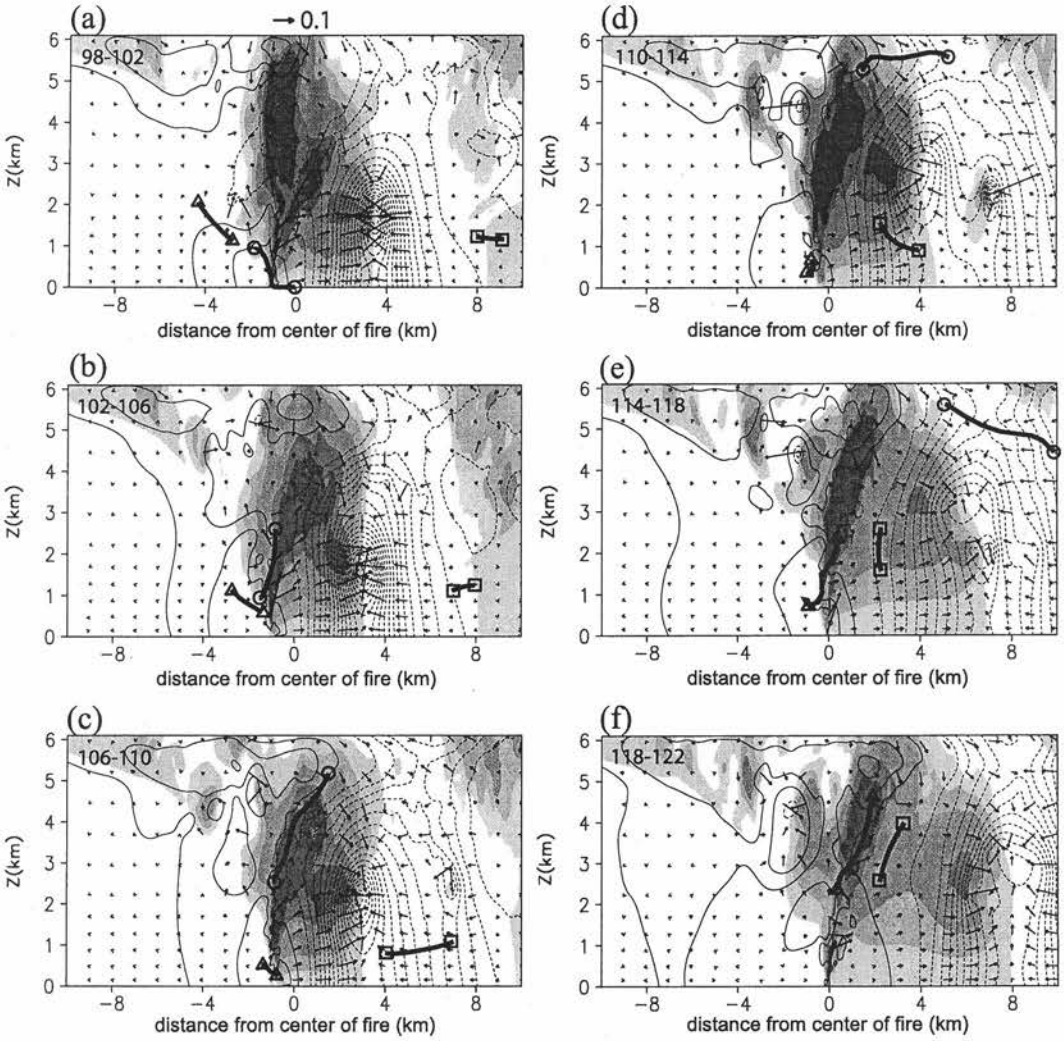

FIG. 11. As in Fig. 6, but for the A2B2 case with analysis period 98–122 s. All figures are in a frame of reference moving with the fire.

organizational mode in high- and low-shear areas of the parameter space.

1) CONSTANT B CONVECTION STATISTICS

Time series of w_{max} and $\overline{M}$ for the B8 and B9 (high B) columns of the experiment matrix indicate less sensitivity of updraft strength to advection when surface buoyancy is held constant (Fig. 17, Table 3) compared to cases in which buoyancy is varied while mixed layer advection is fixed (cf. Figs. 4 and 9). This suggests that buoyancy of surface air parcels exiting the heating region is the primary factor controlling the strength of updrafts, whereas advection through the mixed layer is the discriminating factor for basic convective mode (i.e., plume versus multicell). Cases with quiescent base state profiles (i.e., cases with $A \leq 0.5$ in Fig. 17 and Table 3), however, do not conform to this observation; updrafts under quiescent conditions are 5–7 m s^{-1} stronger than any of the other cases. Also, time series of $\overline{M}$ indicate substantial sensitivity to mixed layer advection when comparing the $A \leq 0.5$ and $A > 2$ cases. The large difference in $\overline{M}$ is largely the result of gyres in the low-advection environment (same phenomenon as in A2B2 case); upward motion within the gyres is included within the domain average mass flux calculation. The amplitude of oscillations in the $\overline{M}$ time series increases with decreasing A, consistent with the increasing unsteadiness as one transitions from the intense plume to the strong multicell mode.

Shifting briefly to the B1 and B2 columns of the parameter space, substantial differences can be seen between cases on either side of the $A = 1$ boundary (Fig. 18, Table 4). Caution must be exercised in drawing conclusions from Fig. 18 or Table 4, however, because the

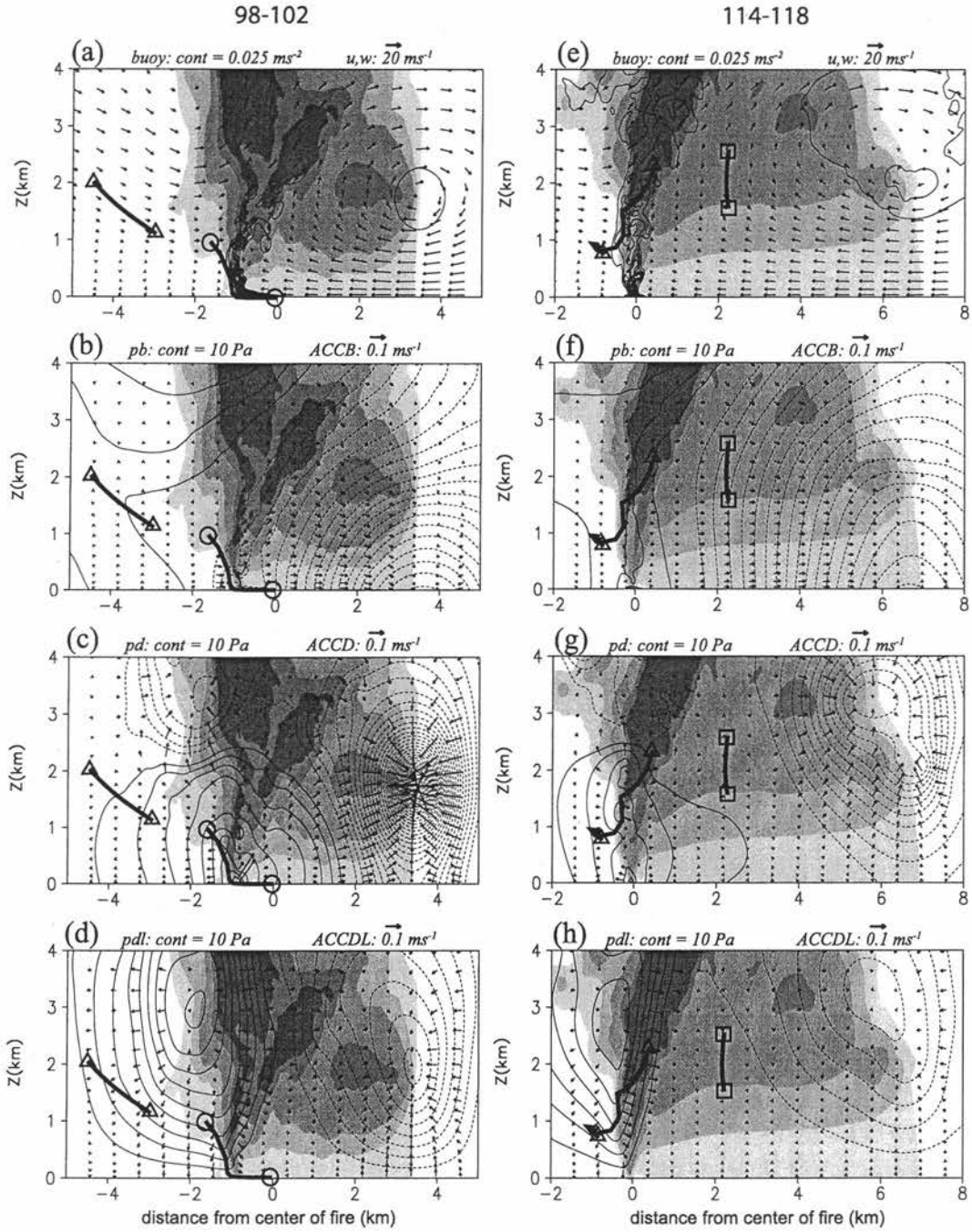

FIG. 12. As in Fig. 7, but for the A2B2 case with analysis periods 98–102 and 114–118 s and with plotting region centered on lower portion of plume. All figures are in a frame of reference moving with the fire.

$A = 1$ boundary separates cases with sharply different wind profiles. Base state wind profiles with $A > 1$ contain modest shear and no wind reversal whereas the base state wind profiles with $A < 1$ exhibit strong shear and low-level wind directions opposite to the mixed layer mean. Generally, the magnitude of the differences in $w_{\max}$ and $\overline{M}$ between high- and low-A cases is much greater for the low-B cases than the high-B cases (cf. Figs. 17 and 18). The increased magnitude of dynamic forcing (associated with the sheared base state wind profile) thus appears to result in a larger disparity between low- and high-A cases. The source of the strong updrafts and large domain-averaged mass fluxes for the low-A, low-B cases was attributed in section 4b

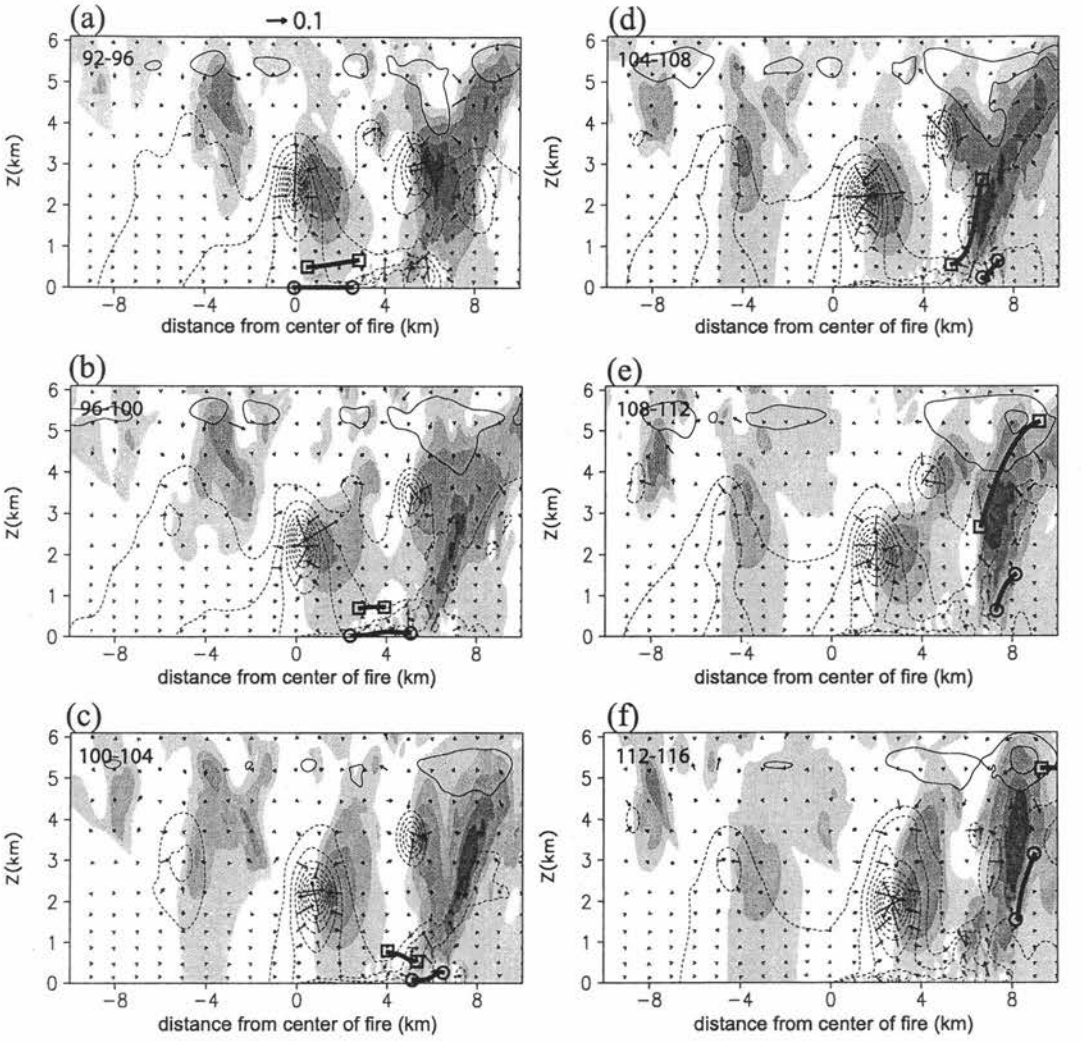

FIG. 13. As in Fig. 6, but for the A2B9 case with analysis period 92–116 s. All figures are in a frame of reference moving with the fire.

to a combination of dynamic pressure gradient forcing and the additional source of air parcels from the upper portion of the mixed layer in the buoyant plume.

2) IMPACT OF WIND REVERSALS ON ADVECTION PROCESS

A relevant question to ask is what role, if any, wind reversals in the base state wind profile play in producing plume (intense plume and hybrid) modes. An examination of the experiment matrix (Fig. 3) reveals that the boundary between plume and multicell, in addition to being collocated with the $A = 1$ critical value, also delineates to a reasonable degree cases with wind reversals (plume) from cases without wind reversals (multicell). To examine whether a wind reversal in the base state wind profile is needed for development of the plume organizational mode, the A2B7 wind profile (plume mode, no wind reversal) was used as a control case for a series of experiments in which parameter B was altered by varying the surface heat flux Q_o rather than the surface wind speed U_s. In each of the experiments, A and B are identical to those cases in the original matrix; however, the wind profile for each experiment is identical to the A2B7 case. If the important aspect of the wind profile for plume versus multicell organization is the A parameter (i.e., mixed layer mean wind speed), then the plume mode should be simulated in all cases because A is less than unity. What is being examined here is whether a wind reversal is required for the most fundamental requirement of the plume classification to

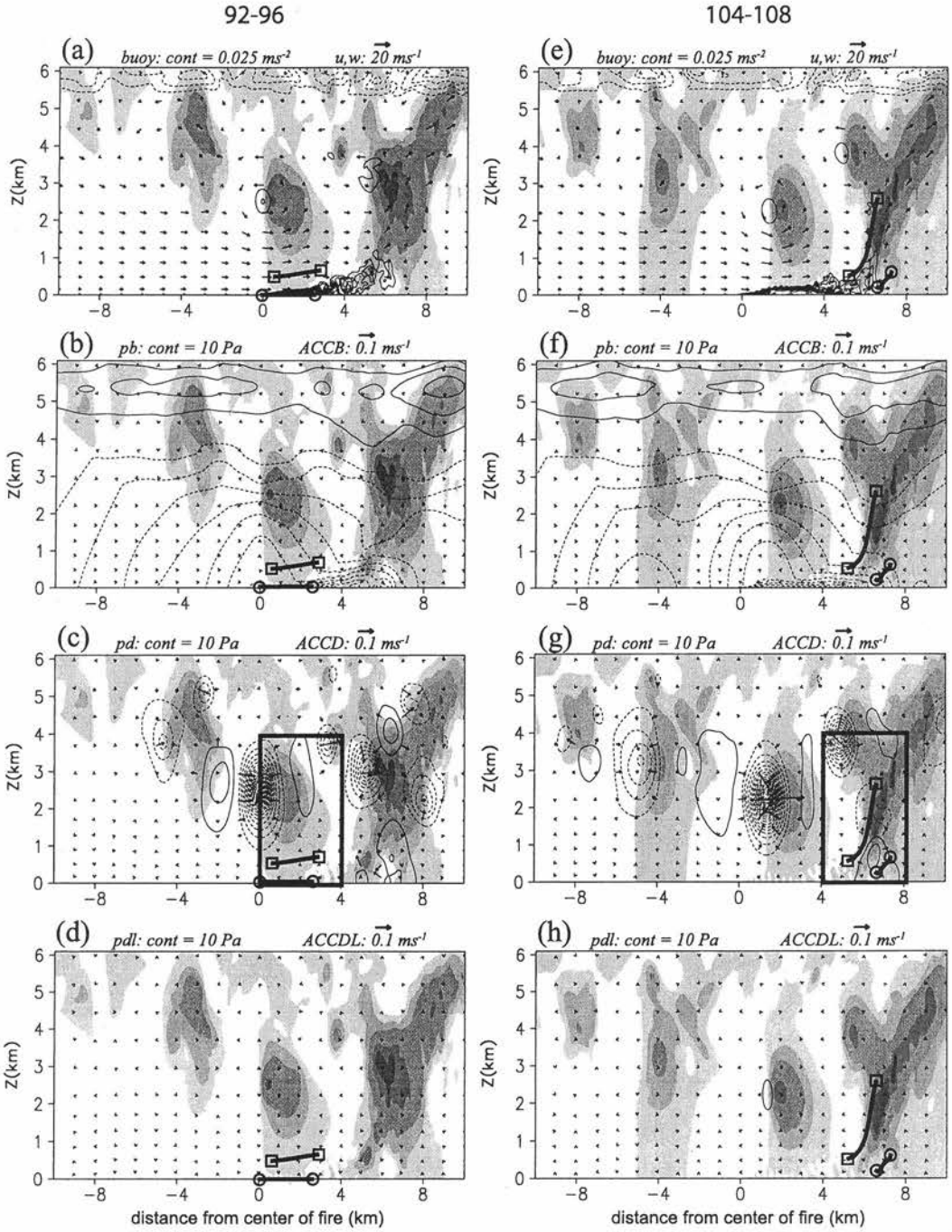

FIG. 14. As in Fig. 7, but for the A2B9 case with analysis periods 92–96 s and 104–108 s. Boxes in (c) and (g) outline the area displayed in Fig. 15. All figures are in a frame of reference moving with the fire.

be met: the absence of new deep convection forming over/near the fire.

Hovmöller diagrams of vertical velocity for the eight cases examined (one control case—A2B7—and seven experiments: A2B1–A2B6 and A2B8) are presented in Fig. 19. In each of the experiments, the organizational mode is definitively plume. A decreasing trend in updraft magnitudes with decreasing parameter B is noted, consistent with the expected decrease in parcel heating. It is also clear that the strength of the upshear and downshear propagating bores weaken as parameter B is decreased. These results support the claim that the

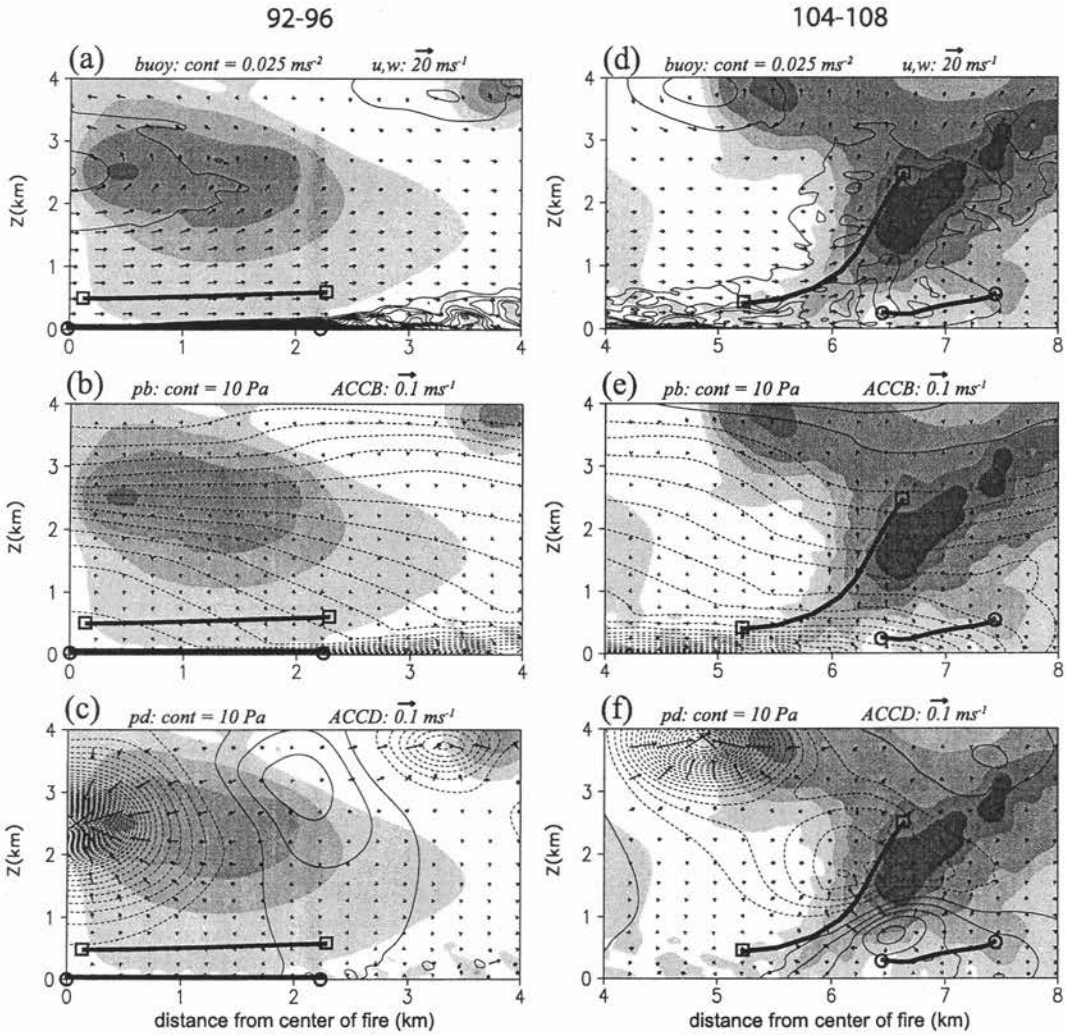

FIG. 15. As in Fig. 14, but for the subset regions indicated there. Linear dynamic perturbation pressure (pdl) panels are omitted. All figures are in a frame of reference moving with the fire.

primary delineator of plume versus multicell organizational mode is parameter A. The results also reinforce the earlier findings that strong background shear and a wind reversal are needed for strong vertical motion in the low-A, low-B cases (i.e., hybrid cases). As discussed earlier, surface parcels in the hybrid cases (e.g., A2B2) approaching the fire traveled beneath a perturbation pressure minimum on the downshear side of the deep updraft (associated with the base state wind shear). Therefore, in the absence of strong shear and a wind reversal, the strength of convection in the low-A, low-B cases was much weaker than in their original counterparts.

A second line of inquiry to be examined is whether multicell convection can consistently be simulated with a base state wind reversal or, in other words, whether the presence of a wind reversal predisposes the mode to be hybrid. In an additional set of experiments, the A2B4 wind profile (with a wind reversal) was modified for each case in the B4 column, keeping the surface wind speed and direction (7.5 m s^{-1}; leftward) constant while adjusting the mixed layer mean wind. The result of these experiments (not shown) was the simulation of multicell convection in the $A > 1$ area of the parameter space, even with a base state wind reversal. This is further confirmation of the importance of parameter A in the organization of plume versus multicell convection.

5. Applications

To a first-order approximation, the background surface wind, relative humidity, and air temperature are the main atmospheric factors that impact fire spread rates (Potter 2002). An increase in surface wind speed directly

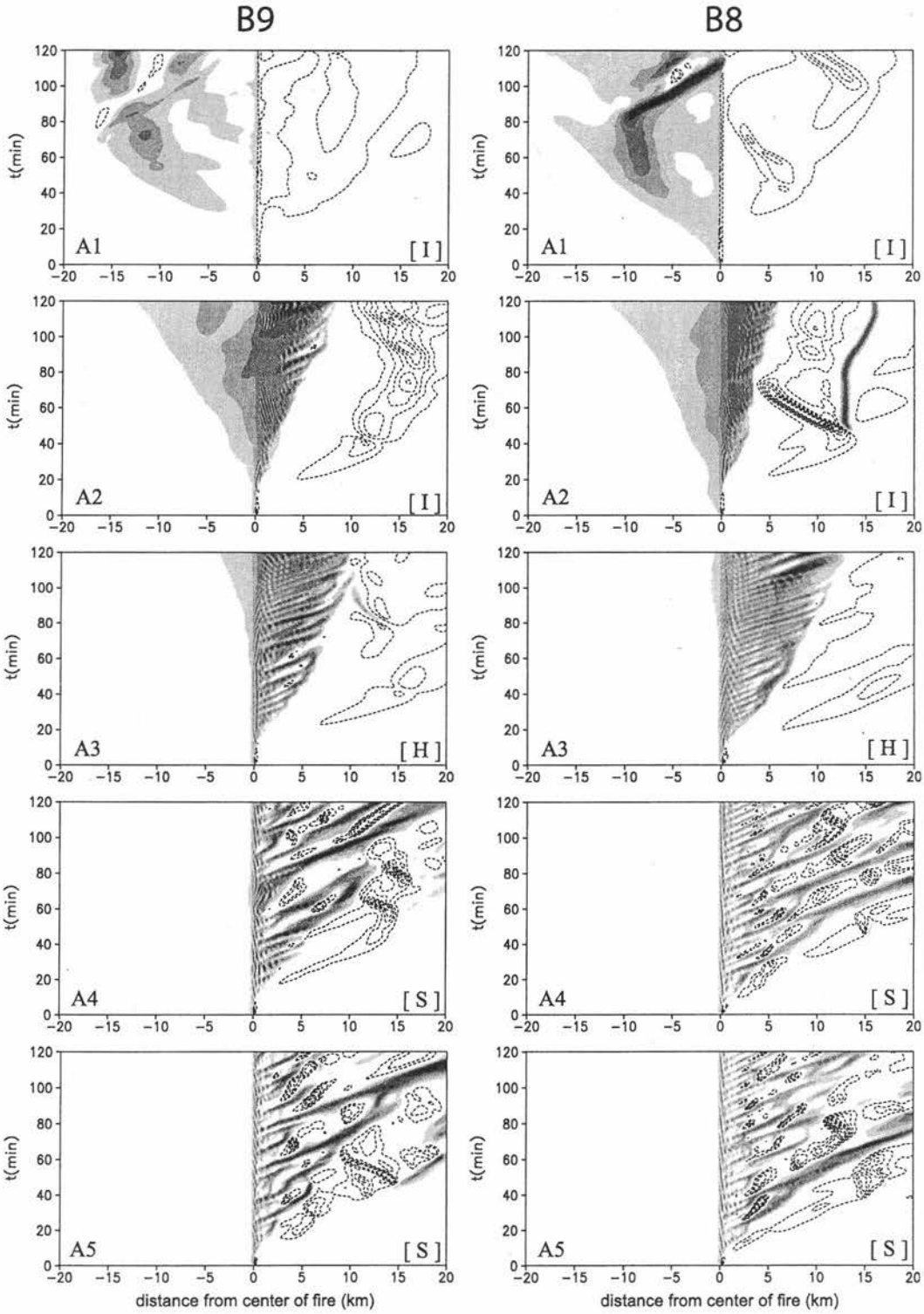

FIG. 16. Hovmöller diagrams of $z = 2.5$ m perturbation horizontal velocity (positive: shaded, negative: short dashed contour; contoured every 3 m s^{-1}) for (left) B9 and (right) B8 cases. A6 cases are omitted because of their similarity to A5 cases. Mode classification as in Fig. 2. All figures are in a frame of reference moving with the fire.

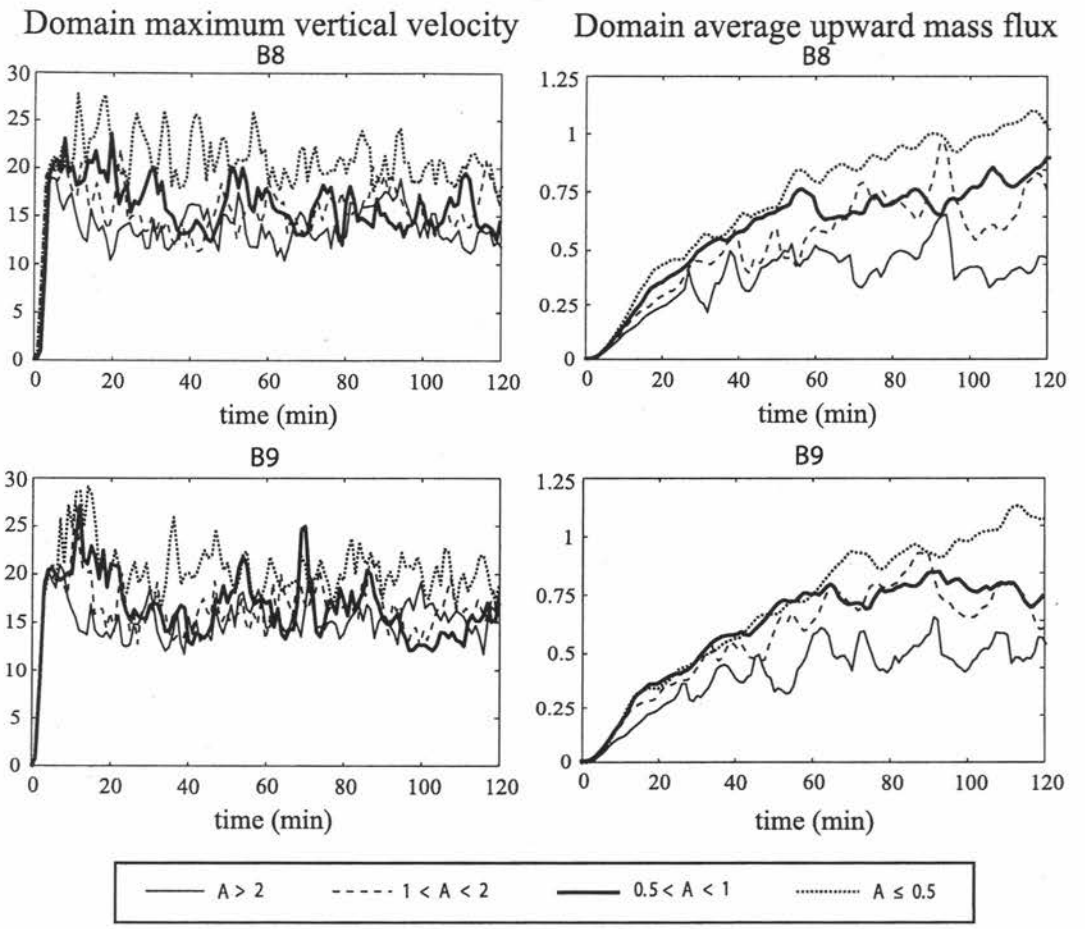

FIG. 17. As in Fig. 4 but for (top) B8 and (bottom) B9 cases. See Table 3 for temporally averaged (t = 40–120 min) values.

enhances fire spread by 1) increasing convective heat transport, 2) tilting flames and soot forward, enhancing radiative heat transfer to unburned fuels, and 3) increasing evaporation of moisture from fuels. A decrease in relative humidity and increase in atmospheric temperature will impact fire spread by enhancing evaporation of moisture from unburned fuels and reducing the amount of heat required for ignition of adjacent fuels, respectively. Secondary, finescale processes that contribute to nonlinear fire behavior have been investigated through both field observations (Clark et al. 1999; Coen et al. 2004; Clements et al. 2007) and numerical modeling (Clark et al. 1996b; Coen 2005; Linn and Cunningham 2005). Small spatiotemporal scale processes, such as generation of finescale vortices and small turbulent eddies, can produce rapidly changing conditions at the fire line that are a major threat to life and property.

This study has identified a number of convective modes that differ substantially in magnitude, vertical scale, and parcel residence time in the vicinity of the heat source. Analyses of perturbation horizontal velocity and potential temperature will be examined for each of the modes to evaluate the potential for fire line variability in different areas of the parameter space. The emphasis of this analysis is on the overall impact of different modes of convection on horizontal wind and potential temperature on the lowest model level (z = 2.5 m). The analysis that follows is not capable of addressing all relevant scales of motion and the model is not designed to explicitly determine changes to fire line structure. Additionally, the reader is reminded that this study has adopted a fire-relative frame of reference.

TABLE 3. As in Table 1, but for cases within the B8 and B9 columns of the experiment matrix.

	$A > 2$	$1 < A < 2$	$0.5 < A < 1$	$A \leq 0.5$
B8	14.4/0.5	15.7/0.6	15.3/0.7	20.5/0.9
B9	15.9/0.6	16.6/0.7	15.9/0.7	20.2/0.9

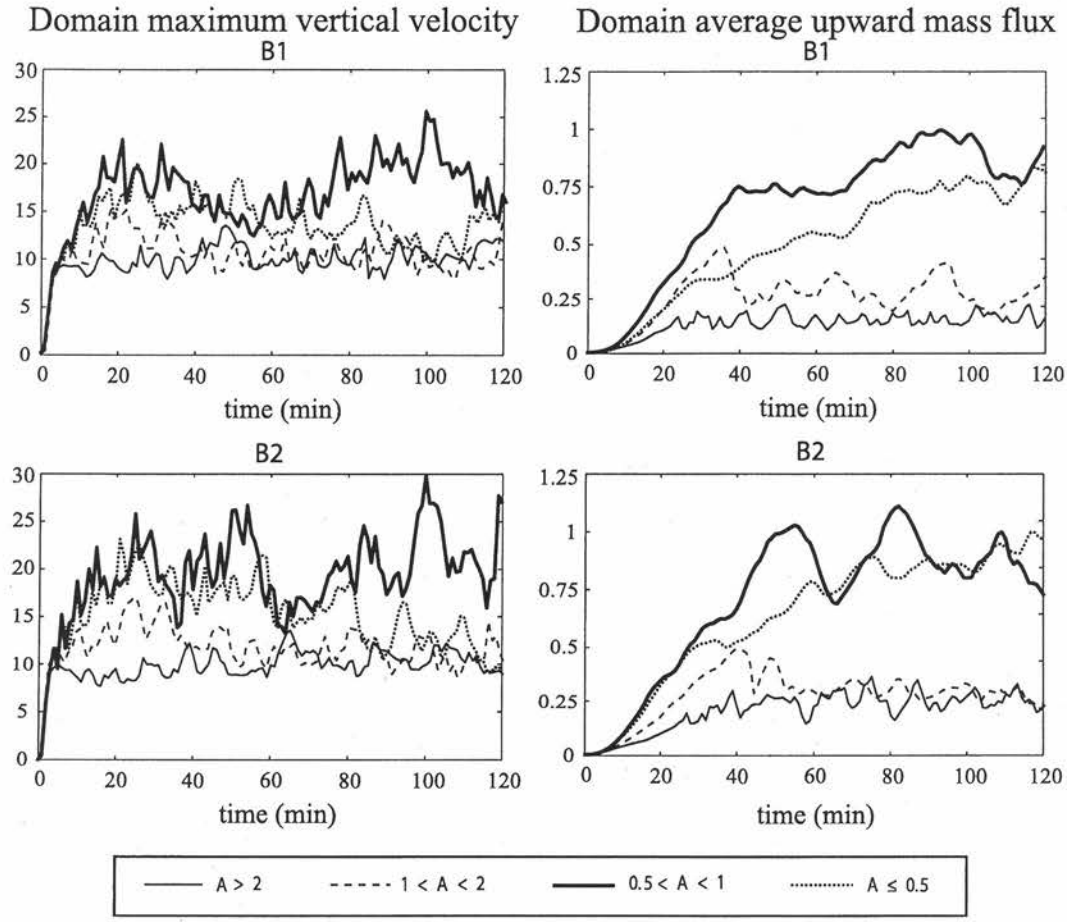

FIG. 18. As in Fig. 4 but for (top) B1 and (bottom) B2 cases. See Table 4 for temporally averaged (t = 40–120 min) values.

Therefore, analyses in this paper consider model fields moving with the fire line at an unspecified, constant speed. An important implication of this framework is that nonlinear processes capable of producing changes to fire spread rates are neglected in favor of the linear processes that are the primary focus of this paper. Future work will address the nonlinear processes that impact the first-order processes identified in this study.

Figures 20 and 21 reveal substantial differences in θ' and u' variability between modes. It is apparent from Fig. 20 that the two low-B (i.e., high U_s) cases generally exhibit the steadiest near-surface θ' on the downstream edge of the heating (Figs. 20b,d), whereas the two high-B (i.e., low U_s) cases feature substantial oscillations with maximum amplitude of 50–60 K (Figs. 20a,c); θ' on the downwind edge of the heating for the strong multicell case (A5B9, Fig. 20c) consists of oscillations with multiple periods (the 1-min period is most obvious). The 1-min period is roughly consistent with the time scale of parcel heating, (i.e., the time it takes for a parcel to cross the heating region). Other frequencies present are probably related to the development of shallow as well as deep cells. However, as discussed earlier, the development of convection is highly aperiodic. The intense plume case (A2B9, Fig. 20a) exhibits oscillatory behavior early in the time series, followed by an extended period of nearly steady θ', consistent with the steady nature of the flow over the heat source during the last 80 min of simulation (e.g., Fig. 6).[1]

Despite the variability associated with the intense plume and strong multicell cases, the hybrid case (A2B2, Fig. 20b) exhibits the most dramatic behavior.

[1] It should be noted that the very high-frequency oscillations seen in the θ' and u' oscillations are not minimally resolved $2\Delta t$ waves because the 5-s sampling period used in constructing the diagrams should be adequate to resolve features with periods of 30 s (the smallest period oscillation in Fig. 20). In any case, the large time step of 0.1 s and application of numerical diffusion supports our assertion that $2\Delta t$ phenomena are not simulated.

TABLE 4. As in Table 1, but for cases within the B1 and B2 columns of the experiment matrix.

	$A > 2$	$1 < A < 2$	$0.5 < A < 1$	$A \leq 0.5$
B1	9.9/0.2	10.6/0.3	17.8/0.8	13.6/0.7
B2	11.3/0.3	11.3/0.3	21.0/0.9	14.9/0.8

A temporary change in surface wind direction at $t = 93$ min and a longer duration occurrence at about 107 min stand out from the otherwise generally steady nature of u' near the heating (Fig. 21). These surface wind changes result in a shift of the position of maximum θ' and weakening of perturbations downwind of the heating (with respect to the basic wind direction). Although the complex oscillations of θ' on the downwind edge of the heating present in the intense plume and strong multicell cases may enhance drying and heating of unburned fine fuels that respond to short-period [O(min)] changes in relative humidity, the most profound impact on fire spread is expected where a wind reversal in the basic flow is present and the plume is steered across the moving fire line (hybrid cases). As a result of the plume crossing the fire line and surface winds reversing direction, forward fire spread would be retarded as heat flux to adjacent fuels weakens.

To summarize the u' behavior, the A5B9 case exhibits complex u' oscillations whereas the A5B2 case exhibits the weakest perturbations and the A2B9 and A2B2 cases undergo distinct transitions in behavior. In terms of impact on fire spread, one would expect fire spread rates for the strong multicell (A5B9) case to exhibit similar periodicity to the u' time series, with fairly smooth fire spread rates for the intense plume and weak multicell case (albeit for different reasons). For the weak multicell case, the steady background wind alone will dominate fire spread rates, whereas for the intense plume case some combination of plume inflow and a bore-induced increase in surface wind speed would also result in a strong, steady fire spread rate. This is unaccounted for if we consider only the role of the background wind in fire spread predictions. The sharp changes in surface wind speed (and direction) for the hybrid case (A2B2) strongly suggest that the environmental wind through the depth of the mixed layer must be considered when determining where convective plumes are likely to move and what their impact on fire spread might be.

6. Summary and conclusions

The fundamental processes controlling the organizational mode and the strength of dry convection generated by wildfires have been examined using two-dimensional idealized atmospheric simulations. Two processes were hypothesized to be important to the problem: heating of air parcels transiting just above the fire and advection of updrafts away from the fire. Dimensional analysis of the fire–atmosphere problem supplied two relevant control parameters: a buoyancy parameter (B) that controls the amount of heat a parcel receives and an advection parameter (A) that controls the advection of updrafts away from the forcing. A set of experiments in which the surface wind speed and mixed layer mean wind speed were varied systematically revealed several organizational modes that exhibit strong sensitivity to the control parameters. The boundary of plume versus multicell was found near $A = 1$, with plume (multicell) modes simulated when $A < 1$ ($A > 1$).

The multicell class was addressed first because of the limited number of overturning wind profiles present in the $A > 1$ area of the parameter space. Note that $w_{\max}$ and $\overline{M}$ statistics indicated stronger and deeper (weaker and more shallow) convection for larger (smaller) B. As the upstream surface wind speed increases (decreases), air parcels transiting the heating receive less (more) heat and penetrate vertically to a lesser (greater) degree as they move downstream. Parcel trajectories revealed the transient nature of the forcing for the strong multicell mode. All of the three investigated surface parcels (released at 4-min intervals) became buoyant upon crossing the heat source and accelerated upward soon thereafter. Updrafts with depths of 1–2 km formed immediately adjacent to the heat source and then translated downstream with little intensification before deepening and intensifying 4–6 km from the source. Decomposition of the pressure field into buoyant and dynamic components indicated that ACCB and ACCDNL contributed approximately equally to upward acceleration. The aperiodicity and highly variable distance from the heat source of deep cell development is consistent with the series of nonlinear splits and mergers that ultimately lead to deep cell development.

Within the low-advection area of the parameter space, the plume class was subdivided into intense plume and hybrid based on whether vertical motion in the upright plume was continuous (intense plume) or consisted of discrete cells (hybrid). Although the majority of plume (intense plume and hybrid) cases examined feature a wind reversal, it was found that plume cases could be consistently simulated without a wind reversal (and multicell cases with a wind reversal), suggesting that parameter A is the main delineator of plume versus multicell. In general, the intense plume mode was simulated when the A (B) parameter was small (large), that is, when surface heating of air parcels was maximized and updrafts were only weakly advected by the

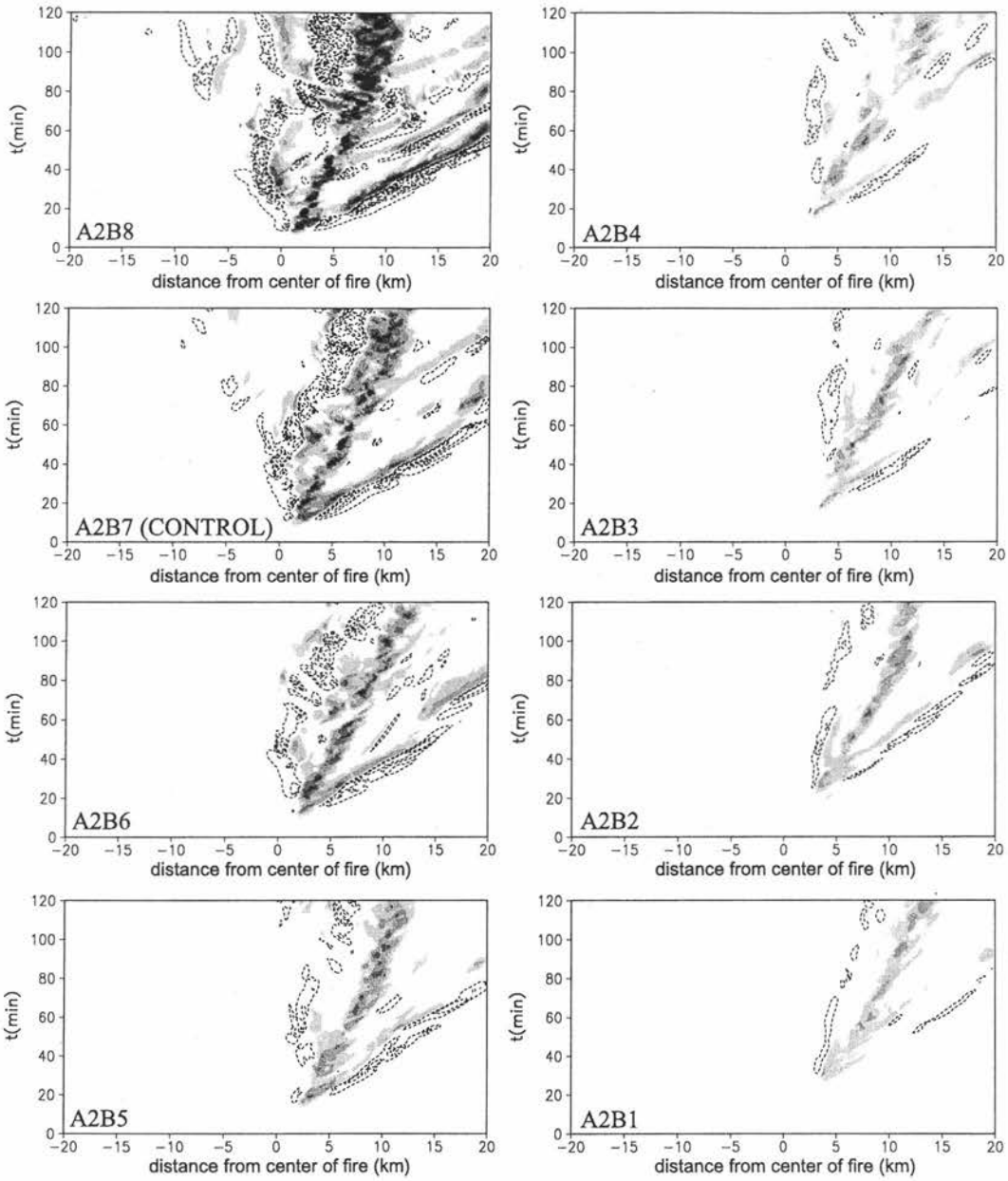

FIG. 19. Hovmöller diagrams of vertical velocity for cases in which parameter B was varied by adjusting surface heat flux Q_o while keeping A constant ($A = 0.3$); A2B7 (CONTROL) experiment included for comparison. All figures are in a frame of reference moving with the fire.

environmental wind. Parcel analysis of the A2B9 case revealed the more steady nature of the intense plume forcing, in which a layer of air about 500 m deep is exposed to buoyant forcing and air parcels ascend into the plume in a smooth manner. The steady nature of the forcing and flow over the heating leads to a nearly hydrostatic state in the lowest 200 m of the model downstream of the heat source, where the buoyant pressure gradient force and BUOY are approximately in balance and vertical acceleration is negligible. Pressure decomposition revealed that acceleration of air parcels into the deep convection was the result of ACCB and ACCDNL, with the latter making the greatest contribution.

The hybrid mode was simulated in cases in which both parameter A and B were small and the base state wind profile exhibited strong shear with a wind reversal. To satisfy the constraints of the two nondimensional parameters, strong shear and reversal of wind direction with height is required where the surface wind speed is

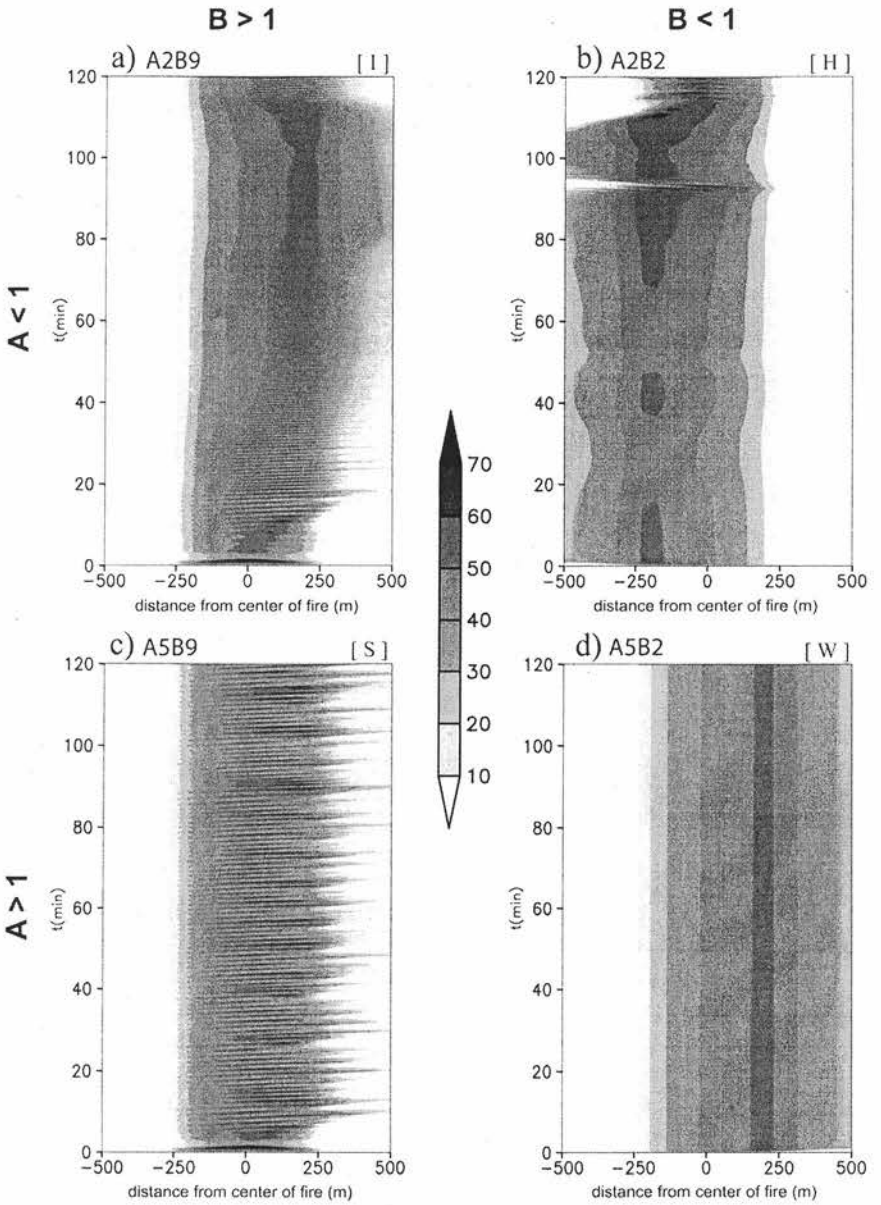

FIG. 20. Hovmöller diagrams of perturbation potential temperature at the lowest model level (z = 2.5 m), for cases (a) A2B9, (b) A2B2, (c) A5B9, and (d) A5B2. Contours are shaded for values greater than 10 K and region ±500 m from fire center is displayed. Mode classification as in Fig. 2. All figures are in a frame of reference moving with the fire.

large but advection averaged through the depth of the mixed layer is small. Parcel analyses for the A2B2 case indicated that unlike the strong multicell or intense plume cases, multiple streams of air parcels ascend through the deep updraft. Air parcels within the topmost 800 m of the mixed layer moving toward the plume descended to as low as 200 m above the surface before rapidly accelerating into the updraft, joining air parcels that had origins in the low levels well upstream of the heat source. Parcel analysis also indicated that air parcels moving toward the plume within the 500–1000-m layer experience upward acceleration due to a perturbation pressure minimum near the center of the mixed layer. The pressure minimum was found to be dynamic in origin, associated in part with the presence of an updraft in base state wind shear. Although parcel analyses of the A2B9 and A5B9 cases indicated contributions from dynamic pressure gradient forcing (mainly nonlinear), the presence of strong and generally steady dynamic forcing in the A2B2 case suggests a greater overall contribution from dynamic

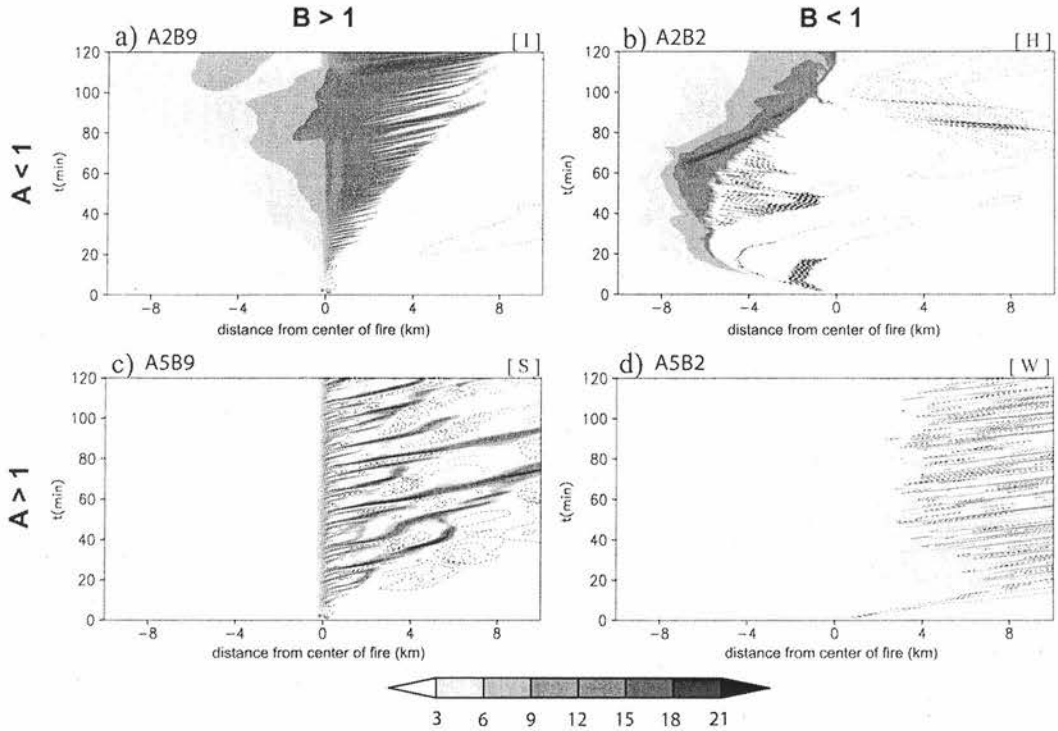

FIG. 21. Hovmöller diagrams of perturbation horizontal velocity at the lowest model level ($z = 2.5$ m), for cases (a) A2B9, (b) A2B2, (c) A5B9, and (d) A5B2. Contours are shaded for values greater than 3 m s^{-1} and region ± 10 km from fire center is displayed. Mode classification as in Fig. 2. All figures are in a frame of reference moving with the fire.

forcing for the hybrid mode. The additional source of air parcels from the upper portion of the mixed layer is further suggestive of a deviation from the basic model of dry convection above forest fires in which air parcels ascending through the plume are forced by buoyancy alone.

The fundamental processes that contribute to development of the intense plume, hybrid, and strong multicell modes are summarized in Fig. 22. In each of the schematics, paths of "typical" air parcels are shown alongside positions of perturbation pressure maxima/minima. The weakness of dynamic forcing associated with base state wind shear is a common trait of the intense plume and strong multicell modes. One crucial difference is apparent, however. In the intense plume class (Fig. 22a), a borelike feature is able to propagate upstream of the fire, owing to the weak mean wind speed, thus permanently altering the low-level horizontal wind speed. Strong vertical gradients of buoyancy and consequently a strong downward-directed pressure gradient force (note bold L_B in Fig. 22a) limit vertical accelerations in the near-hydrostatic inflow. The larger mixed layer mean wind speed associated with the strong multicell case allows no upstream bore propagation, such that low-level flow over the heating remains weak and parcel buoyancy high. The result of this evolution is the development of shallow cells immediately downstream of the heat source (through ACCB), followed by a series of cell splits and merges that ultimately leads to formation of a deep cell. It is important to appreciate that the schematics in Fig. 22 are valid during the later portion of the simulations; even the quasi-steady intense plume case exhibits unsteady behavior during approximately the first 30 min of simulation. In summary, the development of a nearly hydrostatic layer downstream of the heating that resists new cell development is an essential element of intense plume development for cases with nonzero mixed layer advection.

The hybrid mode differs substantially from the other two modes in terms of the presence of an overturning base state wind profile with strong shear. The dynamic component of the pressure gradient force plays a role in the forcing of the mature hybrid mode. The strong mixed layer wind shear is an important component of the dynamic forcing, and the wind reversal allows low-level air parcels to move beneath the dynamic pressure minimum before reaching the heat source. The inability of the two nondimensional parameters to adequately account for such forcing strongly suggests that to be

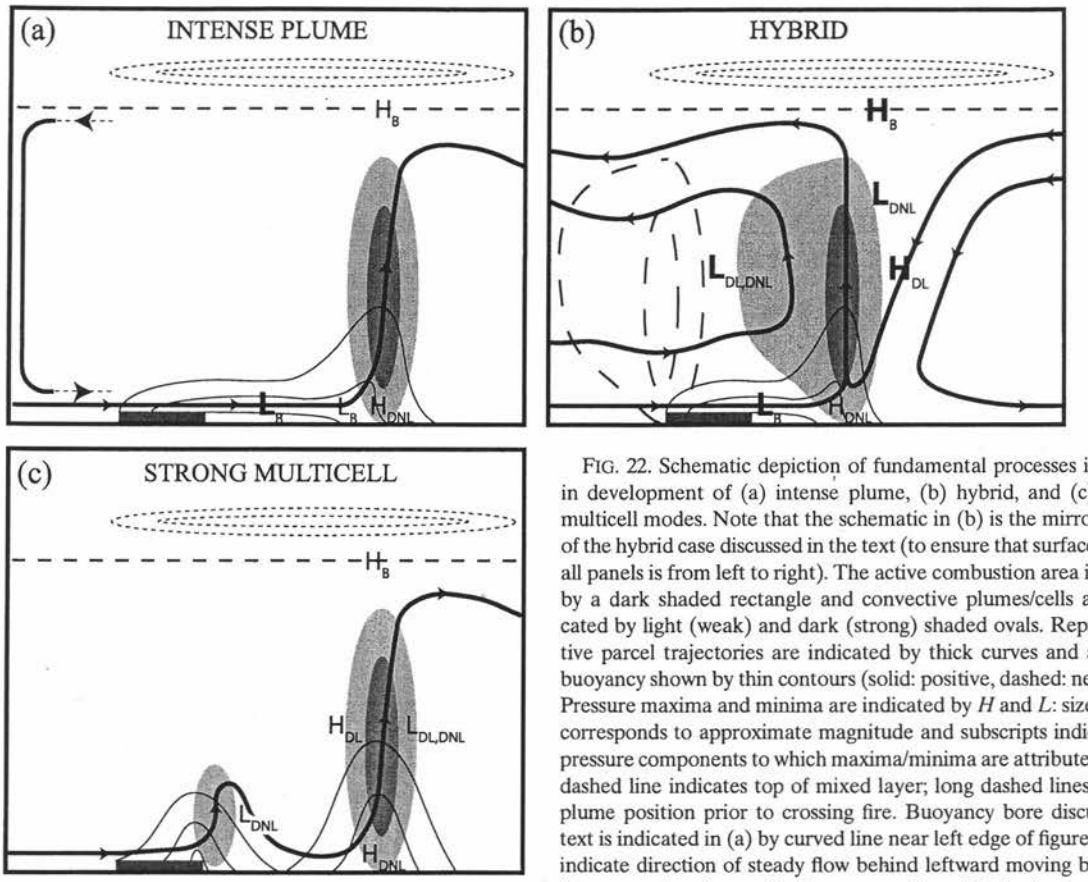

FIG. 22. Schematic depiction of fundamental processes involved in development of (a) intense plume, (b) hybrid, and (c) strong multicell modes. Note that the schematic in (b) is the mirror image of the hybrid case discussed in the text (to ensure that surface flow in all panels is from left to right). The active combustion area is shown by a dark shaded rectangle and convective plumes/cells are indicated by light (weak) and dark (strong) shaded ovals. Representative parcel trajectories are indicated by thick curves and areas of buoyancy shown by thin contours (solid: positive, dashed: negative). Pressure maxima and minima are indicated by H and L: size of font corresponds to approximate magnitude and subscripts indicate the pressure components to which maxima/minima are attributed. Short dashed line indicates top of mixed layer; long dashed lines outline plume position prior to crossing fire. Buoyancy bore discussed in text is indicated in (a) by curved line near left edge of figure; arrows indicate direction of steady flow behind leftward moving bore. All figures are in a frame of reference moving with the fire.

properly applied, additional details of the upstream wind profile must be considered.

The final issue addressed in this paper was the potential impact of the four dry convective modes on the predictability of fire spread. It was noted that the complex oscillations of θ' on the downwind edge of the heating present in the intense plume and strong multicell cases might enhance drying and heating of unburned fine fuels that respond to short-period [O(min)] changes. However, the most profound impact on fire spread is expected when a wind reversal in the basic flow is present and the plume is steered across the moving fire line (hybrid cases). As a result of the plume crossing the fire line and surface winds reversing direction, forward fire spread is retarded because heat flux to adjacent fuels is weakened. Similar conclusions were drawn from the Hovmöller diagrams of u' in Fig. 21. The A5B9 case exhibited oscillations with a number of frequencies whereas the A5B2 case exhibited the weakest perturbations and the A2B9 and A2B2 cases underwent distinct transitions in behavior. In terms of impact on fire spread, it is expected that fire spread rates for the strong multicell (A5B9) case should exhibit similar periodicity to the u' time series, whereas fairly smooth fire spread rates are expected for the intense plume and weak multicell case (albeit for different reasons). For the weak multicell case, the steady background wind alone will dominate fire spread rates; for the intense plume case, some combination of plume inflow and a bore-induced increase in surface wind speed would also result in strong, steady fire spread rates. This would be unaccounted for if only the environmental wind were used in fire spread predictions. Last, the sharp changes to surface wind speed (and direction) for the hybrid case (A2B2) strongly suggests that the background wind through a great depth must be considered when determining where convective plumes are likely to move and what their impact on fire spread might be.

The impact of surface drag on the organizational modes and updraft intensity will be addressed in a future study; great uncertainty in the parameterization of surface drag precluded inclusion in this study. Future work will further examine the dynamics of the apparent bore hypothesized in this study to play an important role in determining plume versus multicell organizational mode. Additional future work will explore three-dimensional processes that impact dry convection forced by quasi-2D fire lines (i.e., fire lines with

gradients of heat flux much weaker in the along-line direction than the cross-line direction). The dynamics of dry convection associated with quasi-2D fire lines need to be explored before considering isolated or area fires that lead to more fully three-dimensional flows. A number of important processes are to be examined, including the impact of tilting of environmental shear by updrafts (Church et al. 1980; Cunningham et al. 2005) and the effect of downdrafts to the rear of the fire line (Sun et al. 2006b) on the dynamics of dry convection. Along a different line, future work will also modify the fire-relative framework to include nonlinear processes, such as inflow into an intense plume enhancing fire spread and turbulent eddies of scale O(m) altering the flux of heat into adjacent fuels. The goal of this future research is to improve understanding of the fundamental two- and three-dimensional processes that control dry convection near forest fires, thus ultimately improving the predictability of rapidly changing (and potentially life-threatening) conditions at the fire line.

Acknowledgments. The first author wishes to thank Dr. Yuh-Lang Lin for proposing the idea of a parameter space study of dry forest fire convection and providing valuable guidance during the early portion of the study. The first author was supported by a National Defense Science and Engineering Graduate (NDSEG) fellowship while performing this research. Computing was performed on the NCSU PAMS Linux cluster and the Army Research Laboratory Linux cluster (MJM).

APPENDIX

Definition of Scales

Scale	Definition
L	Horizontal length scale (m)
L_z	Vertical length scale (m)
U_∞	Upstream horizontal wind speed (m s^{-1})
$\overline{U}$	Mixed layer mean U_∞ (m s^{-1})
U_s	Surface U_∞ (m s^{-1})
w_r	Vertical wind speed scale (m s^{-1})
P'_r	Perturbation pressure scale (Pa)
Q_o	Surface heat flux (W m^{-2})
ρ_o	Base state density (kg m^{-3})
ρ_r	Total density scale (kg m^{-3})
ρ'_r	Perturbation density scale (kg m^{-3})
K_{m_r}	Eddy viscosity coefficient scale (m^2 s^{-1})
K_{H_r}	Eddy diffusivity coefficient scale (m^2 s^{-1})
N^2	Brunt–Väisälä frequency squared (s^{-2})

REFERENCES

Albini, F. A., 1983: Potential spotting distance from burning trees: A predictive model. USDA Forest Service General Tech. Rep. INT-309, 27 pp.

Arya, S. P., 2001: *Introduction to Micrometeorology*. Academic Press, 420 pp.

Baik, J.-J., Y.-H. Kim, and H.-Y. Chun, 2001: Dry and moist convection forced by an urban heat island. *J. Appl. Meteor.*, **40,** 1462–1475.

Banta, R. M., L. D. Olivier, E. T. Holloway, R. A. Kropfli, B. W. Bartram, R. E. Cupp, and M. J. Post, 1992: Smoke-column observations from two forest fires using Doppler lidar and Doppler radar. *J. Appl. Meteor.*, **31,** 1328–1349.

Byram, G. M., 1959: Forest fire behavior. *Forest Fire: Control and Use*, K. P. Davis, Ed., McGraw-Hill, 90–123.

——, 1966: Scaling laws for modeling mass fires. *Pyrodynamics,* **4,** 271–284.

Charney, J. J., and D. Keyser, 2003: Using mesoscale model simulations to better understand the role of surface mixed-layer dynamics in fire–atmosphere interactions. Preprints, *20th Conf. on Weather Analysis and Forecasting/16th Conf. on Numerical Weather Prediction,* Seattle, WA, Amer. Meteor. Soc., 9.5. [Available online at http://ams.confex.com/ams/84Annual/techprogram/paper_69079.htm.]

Church, C. R., J. T. Snow, and J. Dessens, 1980: Intense atmospheric vortices associated with a 1000-MW fire. *Bull. Amer. Meteor. Soc.,* **61,** 682–694.

Clark, T. L., M. A. Jenkins, J. Coen, and D. R. Packham, 1996a: A coupled atmosphere–fire model: Convective feedback on fireline dynamics. *J. Appl. Meteor.,* **35,** 875–901.

——, ——, ——, and ——, 1996b: A coupled atmosphere–fire model: Role of the convective Froude number and dynamic fingering at the fireline. *Int. J. Wildland Fire,* **6,** 177–190.

——, L. Radke, J. Coen, and D. Middleton, 1999: Analysis of small-scale convective dynamics in a crown fire using infrared video camera imagery. *J. Appl. Meteor.,* **38,** 1401–1420.

Clements, C. B., and Coauthors, 2007: Observing the dynamics of wildland grass fires: FireFlux—A field validation experiment. *Bull. Amer. Meteor. Soc.,* **88,** 1369–1382.

Coen, J., 2005: Simulation of the Big Elk Fire using coupled atmosphere–fire modeling. *Int. J. Wildland Fire,* **14,** 49–59.

——, S. Mahalingam, and J. Daily, 2004: Infrared imagery of crown-fire dynamics during FROSTFIRE. *J. Appl. Meteor.,* **43,** 1241–1259.

Cunningham, P., S. L. Goodrick, M. Y. Hussaini, and R. R. Linn, 2005: Coherent vortical structures in numerical simulations of buoyant plumes from wildland fires. *Int. J. Wildland Fire,* **14,** 61–75.

Fovell, R. G., and P.-H. Tan, 1998: The temporal behavior of numerically simulated multicell-type storms. Part II: The convective cell life cycle and cell regeneration. *Mon. Wea. Rev.,* **126,** 551–577.

Grishin, A. M., A. D. Gruzin, and E. E. Gruzina, 1984: Aerodynamics and heat exchange between the front of a fire and the surface layer of the atmosphere. *J. Appl. Mech. Tech. Phys.,* **25,** 889–894.

Heilman, W. E., and J. D. Fast, 1992: Simulations of horizontal roll vortex development above lines of extreme surface heating. *Int. J. Wildland Fire,* **2,** 55–68.

Jenkins, M. A., T. Clark, and J. Coen, 2001: Coupling atmospheric and fire models. *Forest Fire: Behavior and Ecological Effects,* E. A. Johnson and K. Miyanishi, Eds., Academic Press, 257–302.

Kiefer, M. T., Y.-L. Lin, and J. J. Charney, 2008: A study of two-dimensional dry convective plume modes with variable critical level height. *J. Atmos. Sci.,* **65,** 448–469.

Klemp, J. B., 1987: Dynamics of tornadic thunderstorms. *Annu. Rev. Fluid Mech.,* **19,** 369–402.

Lin, Y.-L., R. L. Deal, and M. S. Kulie, 1998: Mechanisms of cell regeneration, development, and propagation within a two-dimensional multicell storm. *J. Atmos. Sci.,* **55,** 1867–1886.

Linn, R. R., and P. Cunningham, 2005: Numerical simulations of grass fires using a coupled atmosphere–fire model: Basic fire behavior and dependence on wind speed. *J. Geophys. Res.,* **110,** D13107, doi:10.1029/2004JD005597.

——, J. Reisner, J. J. Colman, and J. Winterkamp, 2002: Studying wildfire behavior using FIRETEC. *Int. J. Wildland Fire,* **11,** 233–246.

Mapes, B. E., 1993: Gregarious tropical convection. *J. Atmos. Sci.,* **50,** 2026–2037.

McRae, D. J., and B. J. Stocks, 1987: Large-scale convection burning in Ontario. Preprints, *Ninth Conf. on Fire and Forest Meteorology,* San Diego, CA, Amer. Meteor. Soc., 23–29.

——, and M. D. Flannigan, 1990: Development of large vortices on prescribed fires. *Can. J. For. Res.,* **20,** 1878–1887.

Nelson, R. M., 1993: Byram's derivation of the energy criterion for forest and wildland fires. *Int. J. Wildland Fire,* **3,** 131–138.

Palmer, T. Y., 1981: Large fire winds, gases and smoke. *Atmos. Environ.,* **15,** 2079–2090.

Potter, B. E., 2002: A dynamics based view of atmosphere–fire interactions. *Int. J. Wildland Fire,* **11,** 247–255.

——, 2005: The role of released moisture in the atmospheric dynamics associated with wildland fires. *Int. J. Wildland Fire,* **14,** 77–84.

Rotunno, R., and J. B. Klemp, 1982: The influence of the shear-induced pressure gradient on thunderstorm motion. *Mon. Wea. Rev.,* **110,** 136–151.

Simard, A. J., D. A. Haines, R. W. Blank, and J. S. Frost, 1983: The Mack Lake fire. USDA Forest Service General Tech. Rep. NC-83, 38 pp.

Stull, R. B., 1988: *An Introduction to Boundary Layer Meteorology*. Kluwer Academic, 666 pp.

Sun, R., M. A. Jenkins, S. K. Krueger, W. Mell, and J. J. Charney, 2006a: An evaluation of fire-plume properties simulated with the Fire Dynamics Simulator (FDS) and the Clark coupled wildfire model. *Can. J. For. Res.,* **36,** 2894–2908.

——, S. K. Krueger, M. A. Zulauf, M. A. Jenkins, and J. J. Charney, 2006b: Wildfire evolution in the convective boundary layer. Preprints, *17th Symp. on Boundary Layers and Turbulence,* San Diego, CA, Amer. Meteor. Soc., 1.8A. [Available online at http://ams.confex.com/ams/pdfpapers/111198.pdf.]

——, ——, M. A. Jenkins, M. A. Zulauf, and J. J. Charney, 2009: The importance of fire–atmosphere coupling and boundary-layer turbulence to wildfire spread. *Int. J. Wildland Fire,* **18,** 50–60.

Turner, J., 1973: *Buoyancy Effects in Fluids*. Cambridge University Press, 367 pp.

Werth, P., and R. Ochoa, 1993: The evaluation of Idaho wildfire growth using the Haines index. *Wea. Forecasting,* **8,** 223–234.

Xue, M., K. K. Droegemeier, and V. Wong, 2000: The Advanced Regional Prediction System (ARPS)—A multi-scale non-hydrostatic atmosphere simulation and prediction model. Part I: Model dynamics and verification. *Meteor. Atmos. Phys.,* **75,** 463–485.

——, D. Wang, J. Gao, K. Brewster, and K. K. Droegemeier, 2003: The Advanced Regional Prediction System (ARPS), storm-scale numerical weather prediction and data assimilation. *Meteor. Atmos. Phys.,* **82,** 139–170.